Investigation of high-pressure turbulent jets using direct numerical simulation

Nek Sharan[1] **and Josette Bellan**[1,2]

[1]California Institute of Technology, Pasadena, CA 91125, USA
[2]Jet Propulsion Laboratory, California Institute of Technology, Pasadena, CA 91109, USA

(Received xx; revised xx; accepted xx)

Direct numerical simulations of free round jets at a Reynolds number (Re_D) of 5000, based on jet diameter (D) and jet-exit bulk velocity (U_e), are performed to study jet turbulence characteristics at supercritical pressures. The jet consists of Nitrogen (N_2) that is injected into N_2 at same temperature. To understand turbulent mixing, a passive scalar is transported with the flow at unity Schmidt number. Two sets of inflow conditions that model jets issuing from either a smooth contraction nozzle (laminar inflow) or a long pipe nozzle (turbulent inflow) are considered. By changing one parameter at a time, the simulations examine the jet-flow sensitivity to the thermodynamic compressibility factor (Z), inflow condition, and pressure (p) spanning perfect- to real-gas conditions. The inflow affects flow statistics in the near-field (containing the potential core closure and the transition region) as well as further downstream (containing fully-developed flow with self-similar statistics) at both atmospheric and supercritical p. The sensitivity to inflow is larger in the transition region, where the laminar-inflow jets exhibit dominant coherent structures that produce higher mean strain rates and higher turbulent kinetic energy than in turbulent-inflow jets. Decreasing Z at a fixed supercritical ambient pressure (p_∞) enhances pressure and density fluctuations (non-dimensionalized by local mean pressure and density, respectively), but the effect on velocity fluctuations depends also on local flow dynamics. When Z is reduced, large mean strain rates in the transition region of laminar-inflow jets significantly enhance velocity fluctuations (non-dimensionalized by local mean velocity) and scalar mixing, whereas the effects are minimal in jets from turbulent inflow.

Key words: turbulent round jets; high-pressure conditions; supercritical mixing; direct numerical simulation

1. Introduction

Fuel injection and turbulent mixing in numerous applications, *e.g.* diesel, gas turbine, and liquid-rocket engines, occur at pressures and temperatures that may exceed the critical values of injected fuel and oxidizer. At such high pressure (high p), species properties are significantly different from those at atmospheric p. Flow development, mixed-fluid composition and thermal field evolution under supercritical p is characterized by strong non-linear coupling among dynamics, transport properties, and thermodynamics (e.g. Okong'o & Bellan 2002*b*; Okong'o *et al.* 2002; Masi *et al.* 2013) that influences power generation, soot formation, and thermal efficiency of the engines.

The current state-of-the-art in modeling such flows is considerably more advanced than the experimental diagnostics that may produce reliable data for model evaluation

under such conditions. Indeed, high-order turbulence statistics at engine-relevant high-p conditions are difficult to measure and, as of now, remain unavailable. Table 1 lists a sample of supercritical round-jet experimental studies and the flow conditions considered in those experiments. All studies provide only a qualitative assessment of the jet-flow turbulence, highlighting the challenge of obtaining high-fidelity measurements under these conditions. Additionally, several input parameters necessary to perform corresponding numerical simulations are not always reported. Accurate simulations not only require a careful choice of equation of state, multi-species mass and thermal diffusion models, and, at high-Reynolds numbers, subgrid-scale models, but also a matching inflow and boundary conditions to the experiment that are not always available. A large Reynolds number (Re_D) multi-species simulation involves several models, a fact which complicates isolation of individual model errors and a reliable study of jet turbulence characteristics. Moreover, jet turbulence and its sensitivity to flow parameters at supercritical conditions is not well understood even in a simple single-species setting. The present study fills this void by performing direct numerical simulations of single-species round jets at various ambient (chamber) pressure (p_∞), compressibility factor (Z) and inflow conditions.

Effects of (dynamics-based) compressibility, defined in terms of various (convective, turbulence, gradient, deformation) Mach numbers, on free-shear flows have been investigated at perfect-gas conditions in numerous studies, e.g. Papamoschou & Roshko (1988), Lele (1994), Vreman *et al.* (1996), Freund *et al.* (2000) and Pantano & Sarkar (2002). In general, an increase in this compressibility, referred to here as dynamic compressibility, is associated with reduced turbulence kinetic energy (t.k.e.) and reduced momentum-thickness growth rate in shear layers. The reduction is attributed to decrease in t.k.e production resulting from reduced pressure fluctuations in the pressure-strain term (Vreman *et al.* 1996). For homogeneous shear flow, the rapid-distortion-theory results of Simone *et al.* (1997) showed that the t.k.e. change with dynamic compressibility depends on a non-dimensional time based on the mean strain rate. These studies also found that dynamic compressibility influences t.k.e. largely by altering the 'structure' of turbulence and less so by the dilatational terms in the t.k.e. equation. Real-gas effects at high pressure introduce a different type of compressibility, a thermodynamics-based compressibility characterized by

$$Z \equiv \frac{p}{(\rho R_{\mathrm{u}} T/m)}, \tag{1.1}$$

where ρ is the density, T denotes the temperature, R_u is the universal gas constant and m is the species molar mass. In this study, the effects of compressibility changes, using Z, on jet spread rate and t.k.e. production are examined to determine the physical mechanism by which changes in Z influence jet-flow turbulence.

Turbulent free-shear flow computations are sensitive to the choices of initial/inflow conditions, domain size and numerical discretization (Balaras *et al.* 2001; Mattner 2011; Sharan *et al.* 2018*a*). In particular, several experimental (e.g. Wygnanski *et al.* 1986; Slessor *et al.* 1998; Mi *et al.* 2001) and computational (e.g. Ghosal & Rogers 1997; Boersma *et al.* 1998; Grinstein 2001) studies have observed near- as well as far-field flow sensitivity to inflow conditions, supporting the theoretical arguments of George (1989) on existence of various self-similar states determined by the initial/inflow condition. Experimental jet-flow studies typically use a smooth contraction nozzle or a long straight pipe to initialize jet flows (Mi *et al.* 2001). The smooth contraction nozzle produces a laminar inflow with 'top-hat' velocity profile, whereas the long straight pipe produces a fully-developed turbulent inflow. Both inflow cases are studied here, first, to examine the

Reference	Species (injected + chamber)	U_0 (m/s)	$T_{r,ch}$	$T_{r,inj}$	$P_{r,ch}$	$P_{r,inj}$	$Re_D \times 10^3$ $(\rho_e U_e D/\mu)$
Newman & Brzustowski (1971)	$LCO_2 + CO_2/N_2$	2.0 - 4.0	0.97 - 1.09	0.97	0.86 - 1.23	NA	$\sim$ 20 - 30
Woodward & Talley (1996)	$LN_2 + N_2/He$	$\sim$ 1.8 - 2.2	2.21 - 2.46	0.70 - 0.91	0.83 - 2.03	NA	3.4 - 4.1
Mayer *et al.* (1998)	$LN_2 + N_2$	1	2.38	0.83	0.59 - 1.18	NA	$\sim$ 18 - 19
		1.3	1.98	0.71	0.83 - 2.03	NA	$\sim$ 21 - 23
	$LN_2 + He$	1.7	2.31	0.66	1.62 - 2.44	NA	$\sim$ 23 - 24
Oschwald & Schik (1999)	$LN_2 + N_2$	5.0 - 20.0	2.36	0.79 - 1.11	1.17 - 1.76	NA	115 - 340
Chehroudi *et al.* (2002)	$LN_2 + N_2$	10.0 - 15.0	2.38	0.71 - 0.87	0.23 - 2.74	NA	25 - 75
Mayer *et al.* (2003)	$LN_2 + N_2$	1.8 - 5.4	2.36	1.0 - 1.11	3.95 - 5.98	NA	$\sim$ 47 - 157
Segal & Polikhov (2008)	Fluoroketone + N_2	7.0 - 25.0	0.66 - 1.07	0.68 - 1.28	0.05 - 1.86	0.2 - 2.2	11 - 42
Roy *et al.* (2013)	Fluoroketone + N_2	7.07 - 30.0	0.69 - 1.09	1.0 - 1.31	1.26 - 1.88	1.34 - 1.98	NA
Falgout *et al.* (2015)	Dodecane + Air	NA	0.7 & 1.4	0.55	1.6 & 3.2	82.55	NA
Muthukumaran & Vaidyanathan (2016*a*,*b*)	Fluoroketone + N_2	0.86 - 7.5	0.82 - 1.03	0.99 - 1.07	0.81 - 1.34	NA	NA
	Fluoroketone + He	0.82 - 19.0	0.82 - 1.05	0.98 - 1.07	0.72 - 1.34	NA	NA
Baab *et al.* (2016, 2018)	n-hexane + N_2	˜ 91	0.58	1.24	1.65	1.81	120
	n-pentane + N_2	76 & 96	0.63	1.28 & 1.13	1.48	1.62 & 1.61	121 - 139
	Fluoroketone + N_2	41 & 72	0.67	1.13	1.34 & 2.11	2.11	172 - 272
Poursadegh *et al.* (2017)	Propane + N_2	NA	0.9 - 1.35	0.9 - 0.93	0.7 - 1.18	4.7	NA
	Propane + N_2	NA	1.35	1.06	1.3	4.7	NA
Gao *et al.* (2019)	RP-3 kerosene + Air	NA	0.45	0.96 - 1.17	0.042	0.84 - 1.88	NA
	N_2 + Air	$\sim$ 254.8 - 2374.2	2.28	4.91 - 6.02	0.029	0.59 - 1.32	$\sim$ 87.7 - 341

TABLE 1. High-pressure round jet experimental studies. U_e = jet-exit bulk velocity, $T_{r,ch}$ = chamber reduced temperature, $T_{r,inj}$ = injectant reduced temperature, $P_{r,ch}$ = chamber reduced pressure, $P_{r,inj}$ = injectant reduced pressure, ρ_e = jet-exit (or injectant) fluid density, NA = not available. $\sim$ denotes values not provided in the reference but deduced from other parameters. Numbers in blue denote reduced chamber conditions based on injectant critical temperature and pressure.

sensitivity of presumably existing self-similar states to thermodynamic conditions and, second, to determine how the effects of p_∞ and Z are influenced by inflow change. While it is well-known that perfect-gas jets attain a self-similar state, the equivalent information for compressible real-gas jets is unclear.

The present study addresses both perfect-gas jet flows, for which theoretical (e.g. Morris 1983; Michalke 1984) and experimental (e.g. Wygnanski & Fiedler 1969; Panchapakesan & Lumley 1993; Hussein *et al.* 1994) results exist, and high-p supercritical jets, for which detailed turbulence statistics similar to those of perfect-gas jets do not exist, as discussed above. Accurate high-p numerical simulations that correctly account for the non-linear coupling of thermodynamic variables with mass and thermal diffusion are challenging. Masi *et al.* (2013) used a multi-species model (previously proposed by Okong'o & Bellan 2002*b*) to account for these non-linear effects and used the model for direct numerical simulation (DNS) of temporal mixing layers. The present study applies that model to single-species spatially-developing jet flows, as a precursor to multi-species jet simulations. The results from this study provide a database to compare and contrast turbulence statistics from anticipated high-p multi-species jet calculations and to initiate studies to validate large-eddy simulation (LES) models for supercritical flows (e.g. Taşkinoğlu & Bellan 2010; Schmitt *et al.* 2010; Selle & Schmitt 2010; Taşkinoğlu & Bellan 2011). A recent single-species round jet DNS study (Ries *et al.* 2017) examined turbulence statistics and heat transport in a supercritical cold jet using the low-Mach-number equations that decouple pressure and density calculation to neglect the acoustic and compressibility effects. In contrast, the present study solves the fully compressible equations for isothermal jets at a variety of thermodynamic and inflow conditions.

The paper is organized as follows. The governing equations for single-species flow at atmospheric and supercritical p_∞ are discussed in §2. The numerical discretization and computational setup are described in §3.1. Details of the boundary conditions and the two inflow conditions considered in this study are provided in §3.2. The results are presented and discussed in §4: a validation of the equation of state and the transport coefficient models at high p is presented in §4.1; §4.2 provides a validation of perfect-gas simulation results against experimental data; an assessment of the effects of p_∞ and Z at a fixed supercritical p_∞ is provided in §4.3; the influence of p_∞ at a fixed Z is examined in §4.4; §4.5 evaluates the effects of inflow change at supercritical p_∞. A discussion of the observed results and conclusions are provided in §5 and §6, respectively.

2. **Flow conditions and governing equations**

Table 2 summarizes the thermodynamic conditions for the present numerical simulations. Various flow conditions are considered to examine influences of high-p thermodynamics and inflow conditions on round-jet flow statistics. All conditions, simply called "cases", simulate single-species N_2 jets issuing into a quiescent chamber at a Re_D of 5000. In each case, the injected and ambient (chamber) fluid temperature and pressure have the same value, i.e., the jet injects into a chamber fluid that is as dense as the injected fluid. Figure 1 shows Z of pure N_2 for a temperature range at $p = 50$ bar and $p = 70$ bar. For Case 2, at the (p_∞, T_∞) conditions, $Z \approx 0.994$; for Case 3, $Z \approx 0.9$; while for Case 4, $Z \approx 0.8$, thus, representing significant departure from perfect-gas behavior. Cases 2 to 4 investigate the effect of Z. Case 5 compared against Case 3 examines the influence of p_∞ at constant Z. Cases 1T, 2T and 4T examine the influence of inflow perturbations through comparisons against Cases 1, 2 and 4, respectively. Numerical results from increasingly finer grid resolutions, denoted by $N_x \times N_y \times N_z$, are used to ensure grid convergence, as discussed in Appendix A. Results from the finest grid simulation of each case are

Case (description)	$N_x \times N_y \times N_z$	p_∞ (bar)	$T_{\rm ch}(=T_{\rm inj})$ (K)	Z	$\mathcal{F}$	Ma_e	Inflow perturbation
1 (atm-p)	$240 \times 216 \times 216$ $320 \times 288 \times 288$ $400 \times 320 \times 320$	1	293	1.0	6.5	0.6	$0.004U_e$ (lam)
2 (high-p (50); $Z \approx 1$)	$240 \times 216 \times 216$ $320 \times 288 \times 288$ $400 \times 320 \times 320$ $480 \times 360 \times 360$	50	293	0.99	309.4	0.58	$0.004U_e$ (lam)
3 (high-p (50); $Z \approx 0.9$)	$400 \times 320 \times 320$ $480 \times 360 \times 360$	50	199	0.9	641.4	0.73	$0.004U_e$ (lam)
4 (high-p (50); $Z \approx 0.8$)	$400 \times 320 \times 320$ $480 \times 360 \times 360$ $560 \times 408 \times 408$	50	170	0.8	895.7	0.82	$0.004U_e$ (lam)
5 (high-p (70); $Z \approx 0.9$)	$400 \times 320 \times 320$ $480 \times 360 \times 360$	70	211	0.9	774.1	0.69	$0.004U_e$ (lam)
1T (atm-p)	$400 \times 320 \times 320$	1	293	1.0	6.5	0.6	pipe-flow turb
2T (high-p (50); $Z \approx 1$)	$400 \times 320 \times 320$	50	293	0.99	309.4	0.58	pipe-flow turb
4T (high-p (50); $Z \approx 0.8$)	$480 \times 360 \times 360$	50	170	0.8	895.7	0.82	pipe-flow turb

TABLE 2. Summary of the parameters for numerical simulations. The subscripts "inj" and "ch" denote the injection and chamber conditions, respectively. $p_{ch} \equiv p_\infty$ and $T_{ch} \equiv T_\infty$. "lam" associated with a inflow perturbation denotes laminar conditions. Suffix "T" in the name of a case, e.g. 1T, 2T and 4T, denotes turbulent inflow cases.

discussed in §4. The significance of factor $\mathcal{F}$ in table 2 is explained in §2.3. The jet-exit Mach number listed in table 2 is $Ma_e = U_e/c_\infty$, where U_e is the jet-exit (inflow) bulk velocity and c_∞ denotes the ambient sound speed. The bulk velocity is formally defined in §3.2.2. To simulate jets with identical inflow mean velocity for a perturbation type (laminar/turbulent), the same value of U_e is used in all cases. Thus the differences in Ma_e result from the variation in c_∞ at different ambient thermodynamic conditions.

The governing equations are the set of conservation equations and the equation of state; this equation set is complemented by the transport properties.

2.1. *Conservation equations*

The compressible flow equations for conservation of mass, momentum, energy, and a passive scalar, solved in this study, are

$$\frac{\partial \rho}{\partial t} + \frac{\partial}{\partial x_j}\left[\rho u_j\right] = 0, \tag{2.2}$$

$$\frac{\partial}{\partial t}\left(\rho u_i\right) + \frac{\partial}{\partial x_j}\left[\rho u_i u_j + p\delta_{ij} - \sigma_{ij}\right] = 0, \tag{2.3}$$

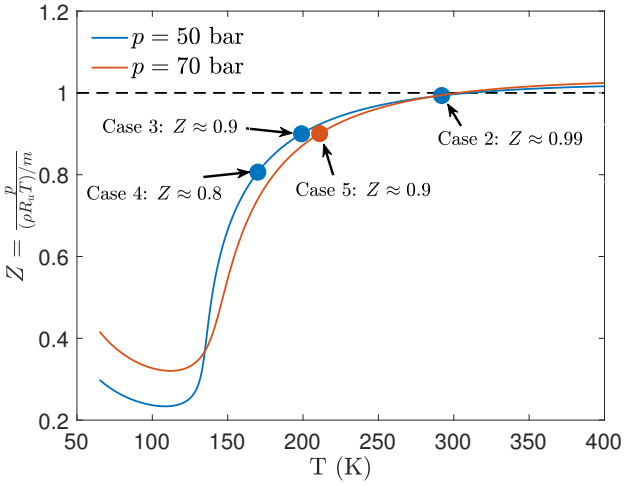

FIGURE 1. Compressibility factor of N_2 at 50 and 70 bar pressure. Blue and red markers denote the chamber conditions for various cases of table 2.

$$\frac{\partial}{\partial t}\left(\rho e_t\right) + \frac{\partial}{\partial x_j}\left[\left(\rho e_t + p\right) u_j - u_i \sigma_{ij} + q_j\right] = 0, \tag{2.4}$$

$$\frac{\partial}{\partial t}\left(\rho \xi\right) + \frac{\partial}{\partial x_j}\left[\rho \xi\ u_j + J_j\right] = 0, \tag{2.5}$$

where t denotes the time, $(x_1, x_2, x_3) \equiv (x, y, z)$ are the Cartesian directions, subscripts i and j refer to the spatial coordinates, u_i is the velocity, p is the pressure, δ_{ij} is the Kronecker delta, $e_t = e + u_i u_i/2$ is the total energy (*i.e.*, internal energy, e, plus kinetic energy), $\xi \in [0, 1]$ is a passive scalar transported with the flow, σ_{ij} is the Newtonian viscous stress tensor

$$\sigma_{ij} = \mu\left(2S_{ij} - \frac{2}{3}S_{kk}\delta_{ij}\right), \qquad S_{ij} = \frac{1}{2}\left(\frac{\partial u_i}{\partial x_j} + \frac{\partial u_j}{\partial x_i}\right), \tag{2.6}$$

where μ is the viscosity, S_{ij} is the strain-rate tensor, and $q_j = -\lambda\, \partial T/\partial x_j$ and $J_j = -\mathcal{D}\, \partial \xi/\partial x_j$ are the heat flux and scalar diffusion flux in j-direction, respectively. λ is the thermal conductivity and $\mathcal{D} = \mu/Sc$ is the scalar diffusivity, where Sc denotes the Schmidt number. The injected fluid is assigned a scalar value, ξ, of 1, whereas the chamber fluid a value of 0. The passive scalar is not a physical species, and is only used as a surrogate quantity to track the injected fluid in this simple single-species flow.

2.2. *Equation of state*

For the near-atmospheric-p simulations (Cases 1 and 1T), the perfect gas equation of state (EOS) is applicable, given by

$$p = \frac{\rho R_{\mathrm{u}} T}{m}. \tag{2.7}$$

For the high-p simulations (Cases 2–5, 2T and 4T), the conservation equations are coupled with a Peng-Robinson (PR) EOS

$$p = \frac{R_{\mathrm{u}} T}{(v_{\mathrm{PR}} - b_{\mathrm{mix}})} - \frac{a_{\mathrm{mix}}}{(v_{\mathrm{PR}}^2 + 2 b_{\mathrm{mix}} v_{\mathrm{PR}} - b_{\mathrm{mix}}^2)}. \tag{2.8}$$

The molar PR volume $v_{\mathrm{PR}} = V - v_{\mathrm{s}}$, where the molar volume $V = m/\rho$. v_{s} denotes

the volume shift introduced to improve the accuracy of the PR EOS at high pressures (Okong'o *et al.* 2002; Harstad *et al.* 1997). a_{mix} and b_{mix} are functions of T and the molar fraction X_α – here $X_\alpha = 1$ – and are obtained from expressions previously published (Sciacovelli & Bellan 2019, Appendix B).

2.3. *Transport properties*

For the near-atmospheric-p simulations (Cases 1 and 1T), the viscosity is modeled as a power law

$$\mu = \mu_R \left(\frac{T}{T_R} \right)^n \tag{2.9}$$

with $n = 2/3$ and the reference viscosity being $\mu_R = \rho_e U_e D/Re_D$, where ρ_e and U_e are the jet-exit fluid density and jet-exit bulk velocity, respectively, and the reference temperature is $T_R = 293\,\mathrm{K}$. The thermal conductivity is $\lambda = \mu C_p/\mathrm{Pr}$, where Prandtl number $\mathrm{Pr} = 0.7$ (as typical of 1 bar flows), the ratio of specific heats $\gamma = 1.4$, and the isobaric heat capacity $C_p = \gamma R_\mathrm{u}/(\gamma - 1)$ is assumed.

For real gases in high-p simulations (Cases 2–5, 2T and 4T), the physical viscosity, μ_ph, and thermal conductivity, λ_ph, are calculated using the Lucas method (Poling *et al.* 2001, Chapter 9) and the Stiel-Thodos method (Poling *et al.* 2001, Chapter 10), respectively. The computational viscosity, μ, and thermal conductivity, λ, are obtained by scaling μ_ph and λ_ph with a factor $\mathcal{F} = \mu_R/\mu_{\mathrm{ph},\infty}$, *i.e.* $\mu = \mathcal{F}\mu_\mathrm{ph}$ and $\lambda = \mathcal{F}\lambda_\mathrm{ph}$, to allow simulations at the specified Re_D of 5000. The ambient physical viscosity ($\mu_{\mathrm{ph},\infty}$) is μ_ph at the pressure p_∞ and the temperature T_ch of respective cases. This procedure ensures that Pr has the physically correct value. The scalar diffusivity is obtained from $\mathcal{D} = \mu/Sc$, where unity Schmidt number is assumed in all cases.

The $\mathcal{F}$ values for all cases are listed in table 2. As an example, for Case 1, $\mathcal{F} = \mu_R/\mu_{\mathrm{ph},\infty} \approx 6.5$ ($\mu_R = \rho_e U_e D/\mathrm{Re}_D = 1.136 \times 10^{-4}\,\mathrm{Pa.s}$ and $\mu_{\mathrm{ph},\infty} = 1.757 \times 10^{-5}\,\mathrm{Pa.s}$ at $p_\infty = 1\,\mathrm{bar}$ and $T_\mathrm{ch} = 293\,\mathrm{K}$), and for Case 2, $\mathcal{F} \approx 309.4$ ($\mu_R = 5.715 \times 10^{-3}\,\mathrm{Pa.s}$ and $\mu_{\mathrm{ph},\infty} = 1.847 \times 10^{-5}\,\mathrm{Pa.s}$ at $p_\infty = 50\,\mathrm{bar}$ and $T_\mathrm{ch} = 293\,\mathrm{K}$). $\mathcal{F}$ is larger in Case 2 compared to Case 1 because of the larger density ρ_e at 50 bar that requires a larger μ_R for a fixed Re_D, while the physical viscosity $\mu_{\mathrm{ph},\infty}$ remains relatively unchanged with increase in p.

3. Numerical aspects

3.1. *Computational domain and numerical method*

For notation simplicity, $(x_1, x_2, x_3) \equiv (x, y, z)$ is adopted for axis labels. (u_1, u_2, u_3) denote the Cartesian velocity components, whereas (u, v, w) denote the axial, radial and azimuthal velocity. The computational domain extends to $42D$ in the axial (x-)direction and $20D$ in the y- and z-direction including the sponge zones, as shown schematically in a x-z plane of figure 2. The boundary conditions are discussed in §3.2.1.

Spatial derivatives are approximated using the sixth-order compact finite-difference scheme and time integration uses the classical explicit fourth-order Runge-Kutta method. To avoid unphysical accumulation of energy at high wavenumbers, resulting from the use of non-dissipative spatial discretization, the conservative variables are filtered every five time steps using an explicit eighth-order filter (Kennedy & Carpenter 1994). The derivative approximations and filter operations over non-uniform stretched grids and polar grids (for post-processing and inflow generation) uses the generalized-coordinate formulation (e.g. Sharan 2016; Sharan *et al.* 2018*b*).

To obtain the numerical solution, the conservation equations are first solved at each

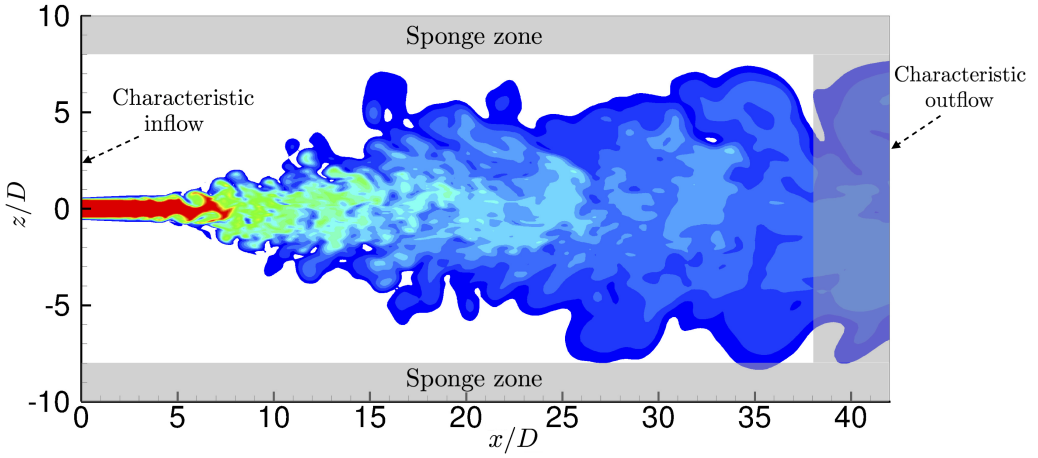

FIGURE 2. A 2D schematic showing the extent of computational domain in axial and radial direction, and the boundary conditions applied at various boundaries.

time step. With ρ and $e = e_t - u_i u_i/2$ obtained from the conservation equations and T computed iteratively from e, the EOS is used to calculate p (Okong'o *et al.* 2002).

3.2. *Boundary and inflow conditions*

3.2.1. *Boundary conditions*

The outflow boundary in the axial direction and all lateral boundaries have sponge zones (Bodony 2006) with non-reflecting outflow Navier-Stokes characteristic boundary conditions (NSCBC) (Poinsot & Lele 1992) at the boundary faces. Sponge zones at each outflow boundary have a width of 10% of the domain length normal to the boundary face. The sponge strength at each boundary decreases quadratically with distance normal to the boundary. The performance of one-dimensional NSCBC (Poinsot & Lele 1992; Okong'o & Bellan 2002*a*) as well as its three-dimensional extension (Lodato *et al.* 2008) by inclusion of transverse terms were also evaluated without the sponge zones; they permit occasional spurious reflections into the domain and, therefore, the use of sponge zones was deemed necessary.

3.2.2. *Inflow conditions*

The role of initial/inflow conditions on free-shear flow development as well as the asymptotic (self-similar) state attained by the flow at atmospheric conditions is well recognized (George & Davidson 2004; Boersma *et al.* 1998; Sharan *et al.* 2019). To examine the high-p jet-flow sensitivity to initial conditions, two types of inflows are considered, portraying either a jet exiting a smooth contracting nozzle or a jet exiting a long pipe. The former produces laminar inflow conditions with top-hat jet-exit mean velocity profile whereas the latter produces turbulent inflow conditions of fully-developed pipe flow (Mi *et al.* 2001).

Cases 1 to 5 model laminar inflow conditions with velocity profile at the inflow plane given by (e.g. Michalke 1984)

$$u(r) = \frac{U_e}{2}\left(1 - \tanh\left[\frac{r - r_0}{2\theta_0}\right]\right), \tag{3.10}$$

where $r = \sqrt{y^2 + z^2}$, the jet exit radius is $r_0 = D/2$ and the momentum thickness is $\theta_0 = 0.04 r_0$. Small random perturbations with maximum amplitude of $0.004 U_e$, as listed in table 2, are superimposed on the inflow velocity profile to trigger jet flow transition to turbulence. Perturbations are only added to the velocity field.

Cases 1T, 2T and 4T model turbulent inflow conditions, typical of jets exiting a long pipe, using the approach of Klein *et al.* (2003), here modified to accommodate circular-pipe inflow geometry. This approach generates inflow statistics matching a prescribed mean velocity and Reynolds stress tensor, using the method of Lund *et al.* (1998), with fine-scale perturbations possessing a prescribed spatial correlation length scale. Thus, the present mean velocity and Reynolds stress profiles are specified from the fully-developed pipe flow DNS results of Eggels *et al.* (1994), where the Reynolds number, based on pipe diameter and bulk velocity, of 5300 is close to the jet Reynolds number of present study. The bulk velocity is defined as

$$U_b = \frac{1}{\pi \left(D/2\right)^2} \int_0^{D/2} 2\pi r u \, \mathrm{d}r. \tag{3.11}$$

$U_b = U_e$ is chosen to keep the same bulk inflow velocity for all cases, irrespective of the inflow condition. The choice of the correlation length scale determines the energy distribution among various spatial scales. Increasing the length scale leads to more dominant large-scale structures. Since the turbulent inflow simulations are aimed at examining influences of fully-developed fine-scale inflow turbulence on jet statistics, a small isotropic value of $L/D = 0.1$ is assumed for the correlation length scale, this value being marginally larger than the finest scale in the velocity spectra of figures 7(a-c) in Eggels *et al.* (1994).

Figures 3 and 4 validate the turbulent inflow implementation. In figure 3, the mean axial velocity from the present turbulent inflow is compared against the pipe flow DNS results (case DNS(E) of Eggels *et al.* 1994). Figure 4 illustrates a similar comparison of the components of Reynolds stress tensor. The overbar ($\bar{\bullet}$) denotes mean quantities, calculated by an average over time and azimuthal (θ) coordinate, given by a discrete approximation of

$$\bar{u}(x, r) = \frac{1}{2\pi} \int_0^{2\pi} \left(\frac{1}{(t_2 - t_1)} \int_{t_1}^{t_2} u(x, r, \theta, t) \mathrm{d}t \right) \mathrm{d}\theta. \tag{3.12}$$

For all results in this study, the time average is performed over time steps in the interval $t_1 = 1000 \leqslant t U_e/D \leqslant 4000 = t_2$.

The method described in Klein *et al.* (2003) assumes a Cartesian grid with uniform spacing, where the periodic directions, along which averages are computed to determine mean quantities, are aligned with the Cartesian directions. The round-jet inflow considered here has circular orifice, where the azimuthal direction is periodic, which is not aligned with a Cartesian direction. Therefore, the fluctuations are computed on a polar grid and, then, interpolated to the Cartesian inflow grid.

4. **Results**

The accuracy of the EOS and the transport coefficient models at supercritical pressure is discussed in §4.1, followed by an examination of atmospheric-p flows, which obey the perfect-gas EOS, in §4.2. The perfect-gas simulations allow validation of the numerical setup through comparisons against experimental results, and also provides a database to

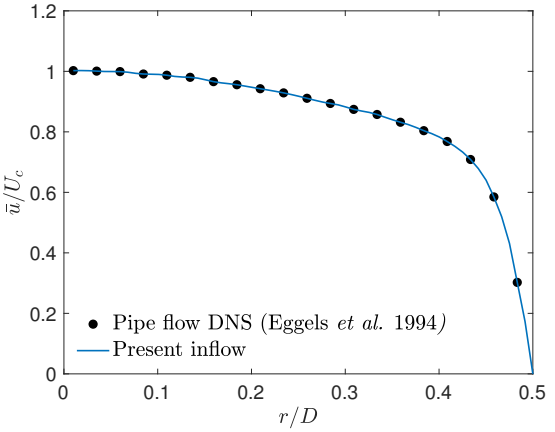

FIGURE 3. Inflow mean velocity normalized by the centerline velocity for the (pseudo-)turbulent inflow compared against the pipe flow DNS results of Eggels *et al.* (1994).

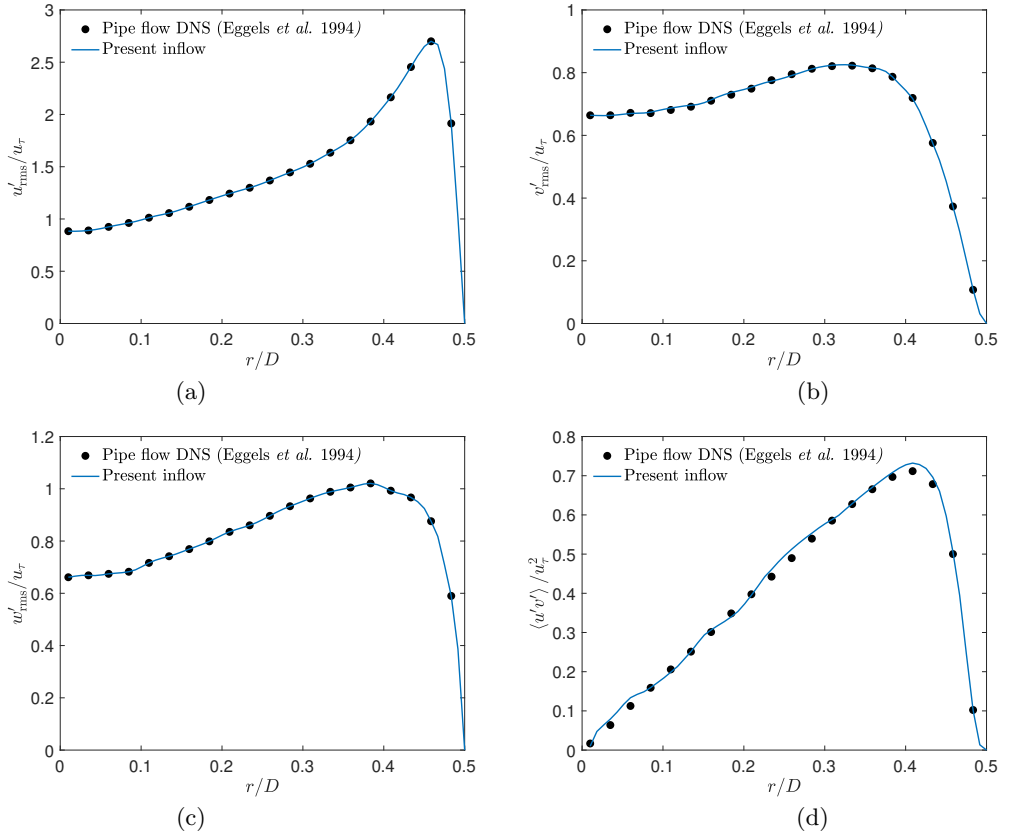

FIGURE 4. Components of Reynolds stress tensor normalized by the wall friction velocity, u_τ, for the (pseudo-)turbulent inflow compared against the pipe flow DNS results of Eggels *et al.* (1994).

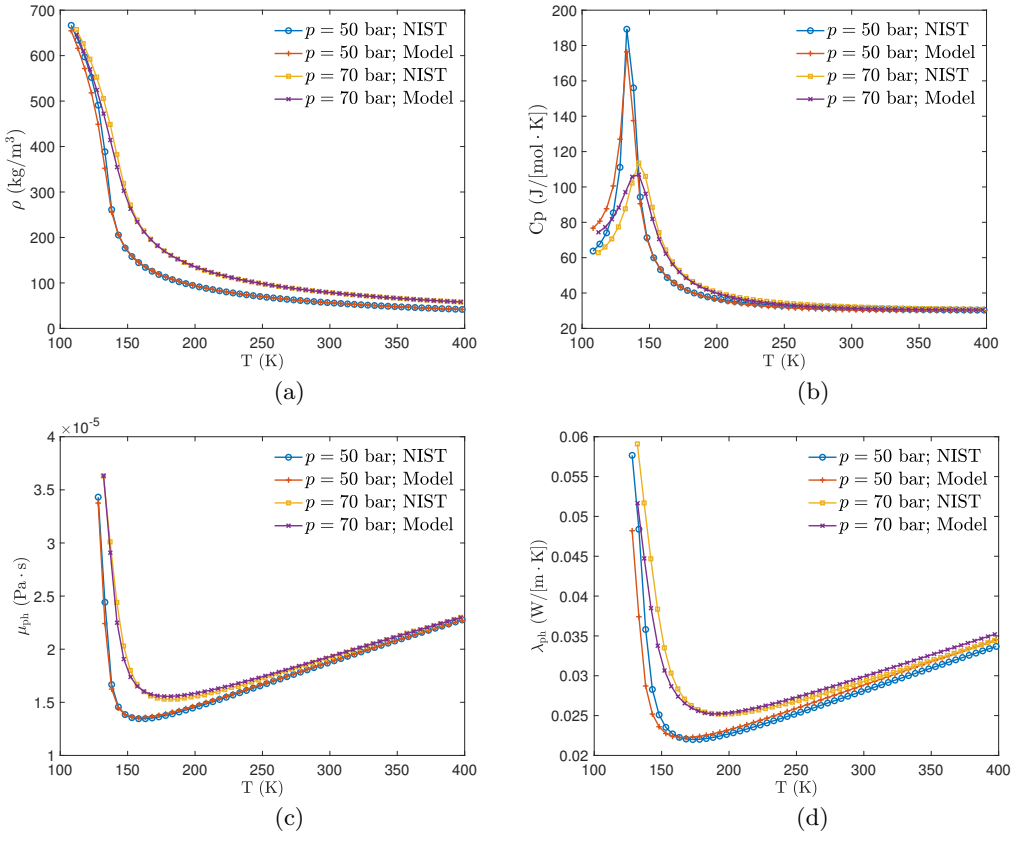

FIGURE 5. EOS and transport coefficients model comparison against NIST database for pure Nitrogen at 50 bar pressure. (a) Density, (b) Isobaric heat capacity, (c) Viscosity, and (d) Thermal conductivity.

compare and contrast with high-p flows, which obey a real-gas EOS, in §4.3, §4.4 and §4.5.

4.1. *Validation of the EOS and transport properties for high-p simulations*

To examine the robustness of the PR EOS and transport coefficient models at supercritical conditions, figure 5 illustrates the density, isobaric heat capacity, and the transport coefficients $\mu_{\rm ph}$ and $\lambda_{\rm ph}$ calculated from the models described in §2.3. The calculated values are compared against the National Institute of Standards and Technology (NIST) database (Lemmon *et al.* 2010) for N_2 at $p = 50$ and 70 bar in the T range 100 K - 400 K, which includes the critical temperature T_{cr} =126.2 K of N_2. As evident, the models have good agreement with the NIST database, showing their validity at high-p conditions. The transport coefficient models are accurate only for $T > T_{cr}$ and, thus, the comparison of $\mu_{\rm ph}$ and $\lambda_{\rm ph}$ only spans this range.

4.2. *Validation of perfect-gas simulations*

4.2.1. *Case 1 results*

Quantitative experimental data for supercritical jets are rare, however, numerous measurements of high-order statistics have been made for jets at atmospheric conditions. For

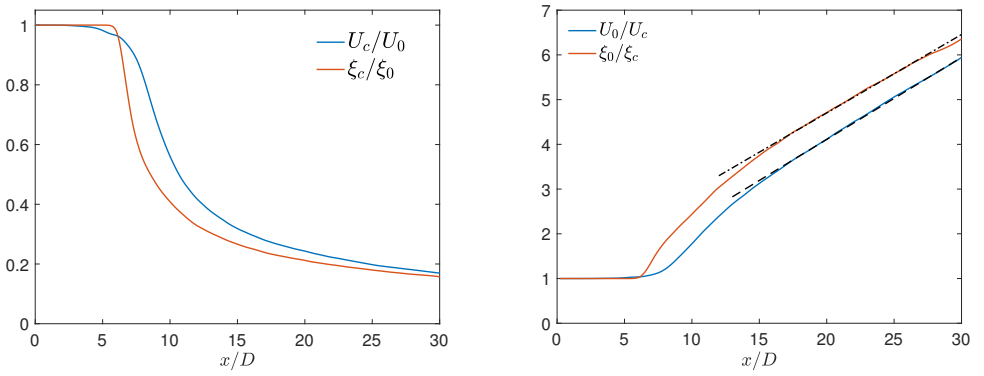

FIGURE 6. Case 1 results: Streamwise variation of the (a) centerline mean velocity (U_c) and scalar concentration (ξ_c) normalized by the respective jet-exit centerline mean values, U_0 and ξ_0, as a function of axial distance and (b) inverse of the normalized time-averaged centerline values showing linear decay asymptotically with axial distance. The dashed line uses $B_u = 5.5$, $x_{0u} = -2.4D$ in (4.13) and the dash-dotted line uses $B_\xi = 5.7$, $x_{0\xi} = -6.8D$ in (4.14).

comparisons, the experimental measurements made in the self-similar region of density-matched jets, where the jet/chamber density ratio is approximately unity, are considered here, e.g. the velocity measurements of Wygnanski & Fiedler (1969), Panchapakesan & Lumley (1993) and Hussein *et al.* (1994), and the passive scalar measurements of Ebrahimi & Kleine (1977), Dowling & Dimotakis (1990) and Mi *et al.* (2001).

Figure 6 shows the decay of the time-averaged centerline velocity, $U_c(x)$, and centerline scalar concentration, $\xi_c(x)$, normalized by the jet-exit centerline velocity, U_0 $(= U_c(0))$, and scalar concentration, ξ_0 $(= \xi_c(0))$, respectively, for Case 1. In the self-similar region, U_c varies with the reciprocal of the downstream distance, given by (e.g. Hussein *et al.* 1994)

$$\frac{U_c\,(x)}{U_0} = B_u \left(\frac{D}{x - x_{0u}} \right), \tag{4.13}$$

where B_u is a constant and x_{0u} denotes the virtual origin derived from the centerline axial velocity. Similarly, the time-averaged centerline scalar concentration has the form

$$\frac{\xi_c\,(x)}{\xi_0} = B_\xi \left(\frac{D}{x - x_{0\xi}} \right), \tag{4.14}$$

where B_ξ is a constant and $x_{0\xi}$ denotes the virtual origin derived from the centerline scalar variation. Simultaneous measurements of the velocity and scalar field in a single experiment were not found in literature and, therefore, data from different studies are used for comparing the velocity and scalar fields. The dashed and dash-dotted lines in figure 6(b) show the profiles for $B_u = 5.5$ and $B_\xi = 5.7$, respectively. They are comparable to the experimentally observed values of $B_u = 5.7$, 6.06 and 5.8 by Wygnanski & Fiedler (1969), Panchapakesan & Lumley (1993) and Hussein *et al.* (1994), respectively, and of $B_\xi = 5.78$ and 5.11 by Ebrahimi & Kleine (1977) and Dowling & Dimotakis (1990), respectively.

Contours of $\langle u \rangle_t / U_0$ in the $y/D = 0$ plane are depicted in figure 7, with dashed lines showing the axial locations where $\bar{u}/U_c$ is plotted in figure 8. The azimuthal averages for calculation of $\bar{u}$ using (3.12) are performed by interpolation of the time-averaged Cartesian-grid solution to a polar grid at respective axial locations. The variation of

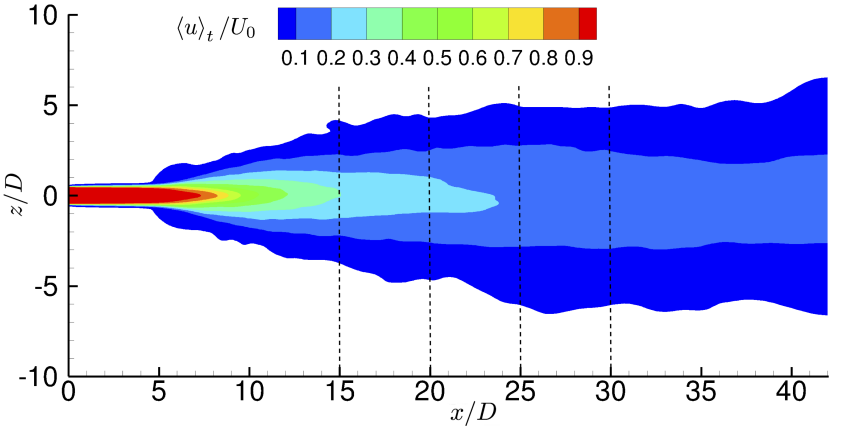

FIGURE 7. Time-averaged axial velocity contours for Case 1. The dashed lines show axial locations where statistics are azimuthally averaged.

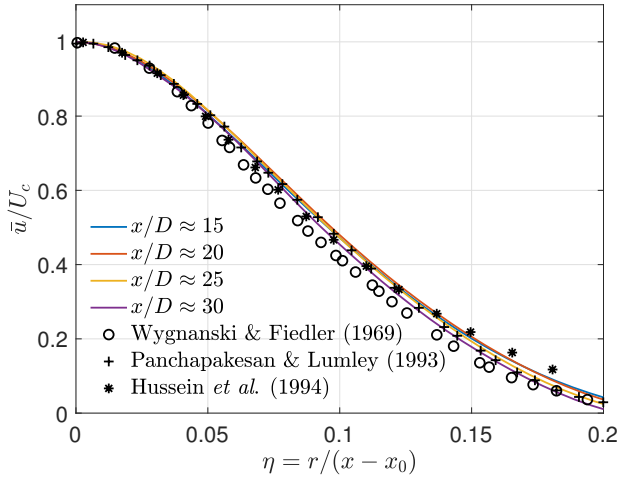

FIGURE 8. Case 1 results: Mean axial velocity ($\bar{u}$) normalized by the centerline mean velocity (U_c) at various axial locations plotted as a function of similarity coordinates compared against the self-similar profiles from the experiments of Wygnanski & Fiedler (1969), Panchapakesan & Lumley (1993) and Hussein *et al.* (1994).

$\bar{u}/U_c$ with the similarity coordinate, $\eta = r/(x - x_{0u})$, is compared with the self-similar profile from experiments in figure 8. The simulation results at various axial locations agree well with each other and with the experimental profile, indicating that the mean axial velocity becomes self-similar around $x/D \approx 15$ for this case.

To further examine the velocity field, figures 9(a)–(c) show the normalized root-mean-square (r.m.s.) fluctuations of velocity components compared against the self-similar profile from experiments. The axial velocity r.m.s. fluctuations are calculated from

$$u'_{\mathrm{rms}} = \sqrt{\left\langle \left\langle \left(u - \langle u \rangle_t \right)^2 \right\rangle_t \right\rangle_\theta} = \sqrt{\left\langle \langle u^2 \rangle_t - \langle u \rangle_t^2 \right\rangle_\theta}, \tag{4.15}$$

where $\langle \cdot \rangle_t$ and $\langle \cdot \rangle_\theta$ denotes the time and azimuthal averages, respectively. A similar definition was applied to compute the radial and azimuthal velocity r.m.s. fluctuations.

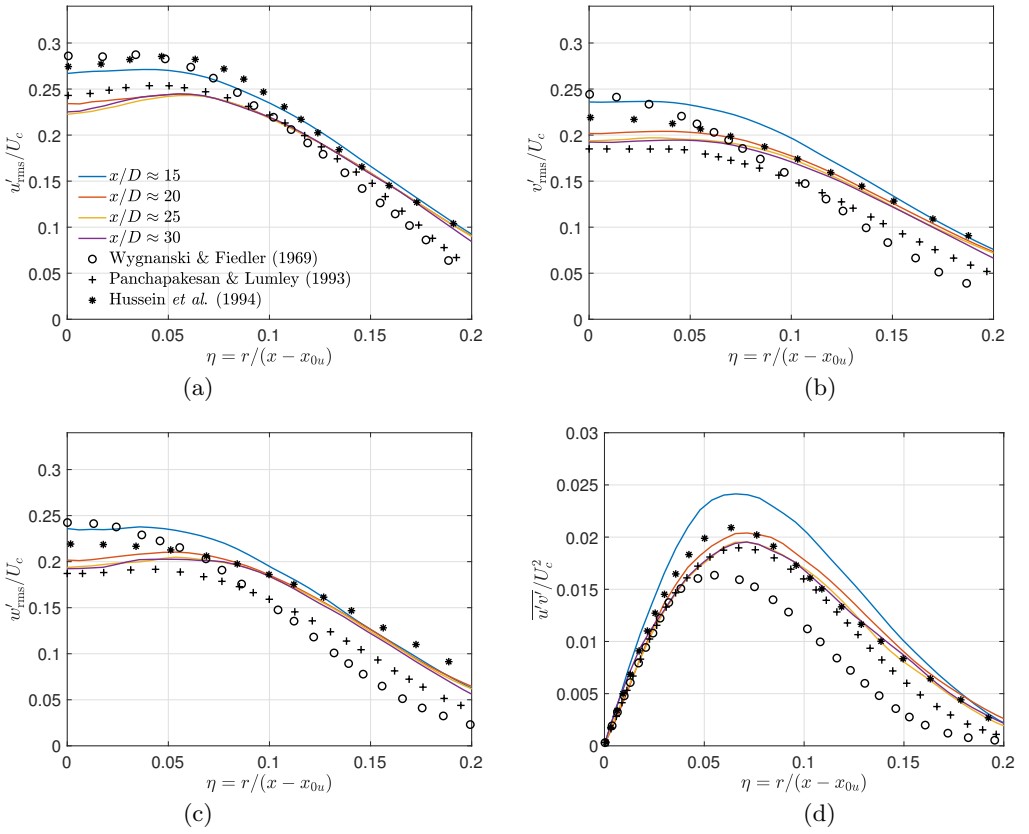

FIGURE 9. Case 1 results: (a) r.m.s. axial velocity fluctuations ($u'_{\rm rms}$), (b) r.m.s. radial velocity fluctuations ($v'_{\rm rms}$), (c) r.m.s. azimuthal velocity fluctuations ($w'_{\rm rms}$) and (d) Reynolds stress ($\overline{u'v'}$) normalized by the centerline mean velocity at various axial locations plotted as a function of similarity coordinates compared against the self-similar profiles from the experiments of Wygnanski & Fiedler (1969), Panchapakesan & Lumley (1993) and Hussein *et al.* (1994). The legend is the same for all plots.

Using the notation $\langle\cdot\rangle_t$ and $\langle\cdot\rangle_\theta$, (3.12) can be written as $\bar{u} = \langle\langle u\rangle_t\rangle_\theta$. Figure 9(d) shows the normalized Reynolds stress, $\overline{u'v'}/U_c^2$, compared against the experimental result. The simulation profiles of normalized r.m.s. fluctuations and Reynolds stress at $x/D \approx 25$ and $x/D \approx 30$, in figure 9, agree well with each other, indicating that these quantities attain self-similarity downstream of $x/D \approx 20$. The simulation self-similar profiles also lie within the experimentally observed self-similar profiles of these quantities.

The self-similarity of the passive scalar field is assessed in figures 10 and 11. $\bar{\xi}/\xi_c$ at various x/D locations is compared against the self-similar profiles of Dowling & Dimotakis (1990) and Mi *et al.* (2001) in figure 10. As evident from the figure, there are minor differences between the profiles at various axial locations, suggesting that the mean scalar concentration is not fully self-similar, but close to self-similarity around $x/D \approx 30$. To further examine the passive scalar behavior, figure 11 shows the scalar r.m.s. fluctuations ($\xi'_{\rm rms}$) with two different normalizations: in figure 11(a) with the mean centerline value (ξ_c), whereas in figure 11(b) with the centerline r.m.s. fluctuation ($\xi'_{c,\rm rms}$). The calculation of centerline averages do not require azimuthal averaging, therefore, $\xi'_{c,\rm rms}$ is calculated

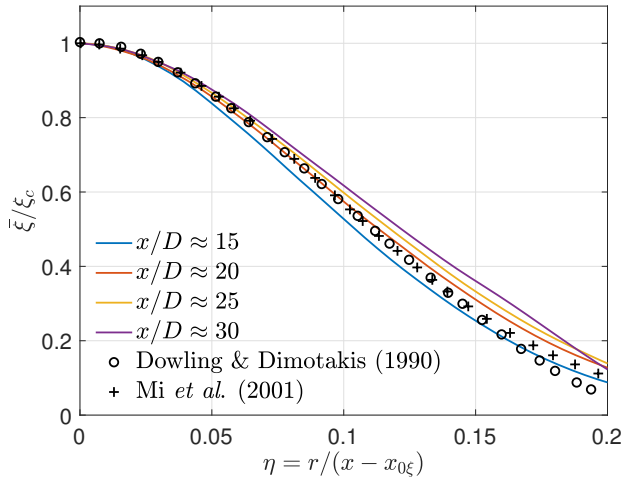

FIGURE 10. Case 1 results: Mean scalar concentration ($\bar{\xi}$) normalized by the centerline mean scalar value at various axial locations plotted as a function of similarity coordinates compared against the self-similar profiles from the experiments of Dowling & Dimotakis (1990) and Mi *et al.* (2001).

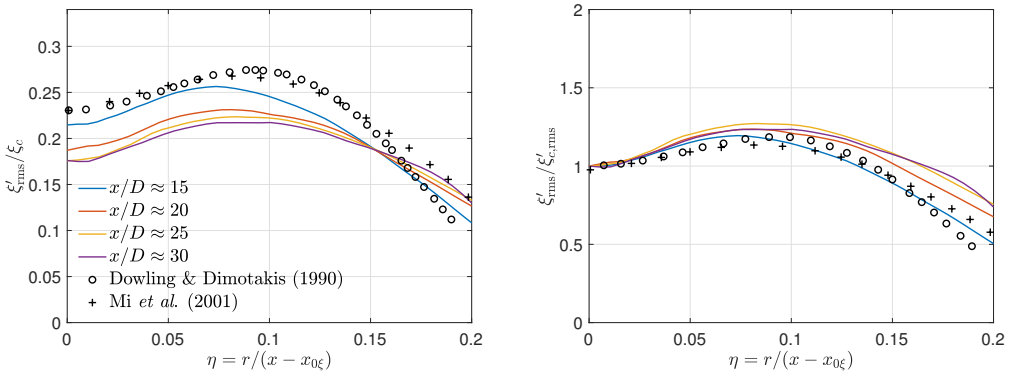

(a) (b)

FIGURE 11. Case 1 results: R.m.s. scalar fluctuations ($\xi'_{\rm rms}$), normalized by the (a) centerline mean scalar value (ξ_c) and (b) centerline r.m.s. scalar fluctuation ($\xi'_{c,\rm rms}$) plotted as a function of similarity coordinates compared against the self-similar profiles from the experiments of Dowling & Dimotakis (1990) and Mi *et al.* (2001). The legend is the same for both plots.

from

$$\xi'_{c,\rm rms} = \sqrt{\left\langle (\xi - \xi_c)^2 \right\rangle_t} = \sqrt{\langle \xi^2 \rangle_t - \xi_c^2}, \tag{4.16}$$

where $\xi_c(x) = \bar{\xi}(x, r = 0)$. A better agreement with the experimental self-similar profiles in figure 11(b), compared to figure 11(a), indicates that $\xi'_{\rm rms}/\xi'_{c,\rm rms}$ attains self-similarity at shorter axial distance than $\xi'_{\rm rms}/\xi_c$.

The favorable comparisons between simulation results and experimental measurements indicate that the governing equations with perturbed laminar inflow and the numerical method accurately simulate the jet exiting a smooth contracting nozzle at atmospheric-p.

4.2.2. *Inflow effects at perfect-gas condition: comparisons of Case 1 and 1T*

The influence of inflow conditions on near- and far-field jet flow statistics at atmospheric conditions has been a subject of numerous investigations, e.g. Husain & Hussain (1979), Richards & Pitts (1993), Boersma *et al.* (1998), Mi *et al.* (2001), Xu & Antonia (2002). Several studies have questioned the classical self-similarity hypothesis (Townsend 1980) that the asymptotic state of the jet flow depends only on the rate at which momentum is added and is independent of the inflow conditions. Those studies support the analytical result of George (1989), who suggested that the flow can asymptote to different self-similar states determined by the inflow condition. It is thus pertinent to use the two inflow conditions described in §3.2.2 to examine the uniqueness of the self-similar state at near-atmospheric p_∞. In contrast to past investigations in which measurements were obtained of either the velocity or the passive scalar field, here the inflow effects on the velocity and the scalar field are simultaneously examined.

Before examining the differences in results from the two inflows, we note that for the laminar inflow, which has a top-hat jet-exit mean velocity profile, $U_e \approx U_0$, whereas for the turbulent inflow, which has a parabolic jet-exit mean velocity profile $U_e < U_0$. The present study uses same value of bulk inflow velocity, U_e, for all simulations, independent of the inflow condition. As a result, the dimensional value of U_0 is different for laminar and turbulent cases.

Figure 12 illustrates the near-field scalar contours from Cases 1 and 1T at $tU_e/D \approx 3500$ (the corresponding full-domain contours are shown in figure 41). The rendered contour lines show the mixed fluid, defined as $0.02 \leqslant \xi \leqslant 0.98$. Evidently, the near-field flow features are considerably different for the two jets. The instabilities in the annular shear layer that trigger vortex roll-ups appear at larger axial distance in the jet from the laminar inflow (Case 1) than those in the jet from the pseudo-turbulent inflow (Case 1T). The inflow disturbances in Case 1T, modeling pipe-flow turbulence, are broadband and higher in magnitude, thus triggering small-scale turbulence that promote axial shear-layer growth immediately downstream of the jet exit. In contrast, the laminar inflow has small random disturbances superimposed over the top-hat velocity profile that trigger the natural instability frequency (Ho & Nosseir 1981) and dominant vortical structures/roll-up around $x/D \approx 5$. The larger axial distance required for the natural instability to take effect in Case 1 leads to a longer potential core than in Case 1T. However, once the instabilities take effect in Case 1, at $x/D \approx 5$, dominant vortical structures close the potential core over a short distance, i.e. around $x/D \approx 8$. In comparison, in Case 1T, the broadband small-scale turbulence triggered immediately downstream of the jet exit closes the potential core around $x/D \approx 6$. Downstream of the potential core collapse, an abrupt increase in the jet width is observed in Case 1, while the jet grows gradually in Case 1T.

The above-discussed qualitative differences are now quantified using various velocity and scalar statistics.

4.2.2.1 Velocity and scalar statistics, and self-similarity

A comparison of U_c and ξ_c axial decay between Case 1 and Case 1T jets is presented in figure 13(a). The shorter potential core length of Case 1T leads to velocity and scalar decay beginning upstream of that in Case 1. The difference between the axial locations where the velocity and scalar begin to decay is noticeable for Case 1, while it is relatively small for Case 1T thus indicating a tighter coupling of dynamics and molecular mixing in Case 1T. The upstream decay of the scalar, with respect to velocity, in the laminar

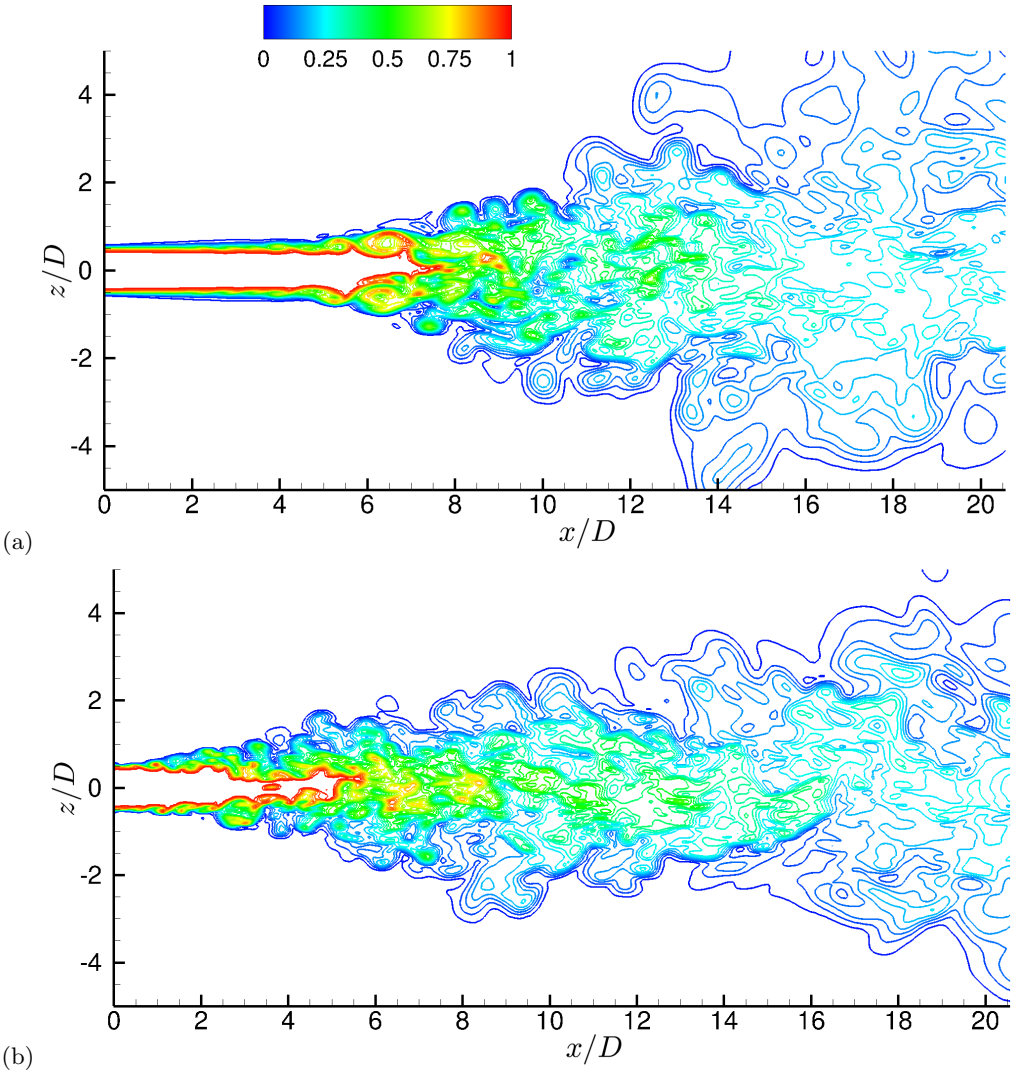

FIGURE 12. Near-field instantaneous scalar contours at $tU_e/D \approx 3500$ from (a) Case 1 and (b) Case 1T showing the mixed fluid concentration. The contour lines show 24 levels in the range $0.02 \leqslant \xi \leqslant 0.98$. The legend is the same for both plots.

inflow jet (Case 1) is consistent with the observation of (Lubbers *et al.* 2001, Figure 6) for a passive scalar diffusing at unity Schmidt number. Also noticeable in the Case 1 results is a transition or development region, $7 \lesssim x/D \lesssim 15$, where the velocity and scalar decay rates are larger than in the asymptotic state reached further downstream. The Case 1T results do not show a similarly distinctive transition region, and the velocity and scalar decay rates remain approximately the same downstream of the potential core closure. Downstream of $x/D \approx 15$, the velocity and scalar decay rates are similar for Cases 1 and 1T: $B_u = 5.5$ ($x_{0u} = -2.4D$) and $B_\xi = 5.75$ ($x_{0\xi} = -3.5D$) for Case 1T, whereas $B_u = 5.5$ ($x_{0u} = -2.4D$) and $B_\xi = 5.7$ ($x_{0\xi} = -6.8D$) for Case 1.

The velocity and scalar half-radius for Cases 1 and 1T are compared in figure 13(b). The solid black lines in figure 13 indicating the spreading rate in the self-similar region

of various cases are given by

$$\text{Case 1:} \qquad r_{\frac{1}{2}u}/D = 0.085\,(x/D + 4.4)\,, \tag{4.17a}$$

$$\text{Case 1:} \qquad r_{\frac{1}{2}\xi}/D = 0.14\,(x/D + 1.5)\,, \tag{4.17b}$$

$$\text{Case 1T:} \qquad r_{\frac{1}{2}u}/D = 0.078\,(x/D + 1.7)\,, \tag{4.17c}$$

$$\text{Case 1T:} \qquad r_{\frac{1}{2}\xi}/D = 0.11\,(x/D + 0.85)\,. \tag{4.17d}$$

The Case 1 jet spreads at a faster rate than Case 1T, consistent with the experimental observations of Xu & Antonia (2002) and Mi *et al.* (2001). The decrease in velocity half-radius spreading rate from 0.085 (Case 1) to 0.078 (Case 1T) is consistent with the observations of Xu & Antonia (2002), where a decrease in spreading rate from 0.095 for the jet issuing from a smooth contraction nozzle to 0.086 for the jet from a pipe nozzle was reported. The spreading rate of 0.14 and 0.11 based on the scalar half-radius for Case 1 and Case 1T, respectively, is larger than the values of 0.11 and 0.102 reported by Mi *et al.* (2001) for their temperature scalar field from smooth contraction nozzle and pipe jet, respectively, but comparable to the values of 0.13 and 0.11 deduced from the results of Richards & Pitts (1993) for their mass-fraction scalar field from smooth contraction nozzle and pipe jet, respectively. The profiles in figure 13 also show that the velocity and scalar mean fields attain self-similarity, i.e. their centerline values decay linearly and the half-radius spreads linearly, at smaller axial distance in Case 1T than in Case 1. In the self-similar region, the U_c and ξ_c decay rates of Cases 1 and 1T are comparable, while the half-radius spreading rates differ considerably.

Further differences between Cases 1 and 1T are documented in figures 14, 15 and 16. Examination of figure 14(a) shows that the mean axial velocity attains self-similarity as near-stream as $x/D \approx 15$ for both Case 1 and 1T, however, the self-similar profiles are different. The self-similar mean velocity/scalar field can be expressed as

$$\bar{u}(x,r) = U_c\,(x)\,f\,(\eta)\,, \qquad \bar{\xi}(x,r) = \xi_c\,(x)\,g\,(\eta)\,, \tag{4.18}$$

where $f\,(\eta)$ and $g\,(\eta)$ are similarity functions, often described by Gaussian distributions,

$$f\,(\eta) = \exp\left(-A_u\eta^2\right), \qquad g\,(\eta) = \exp\left(-A_\xi\eta^2\right), \tag{4.19}$$

where A_u and A_ξ are constants determined from a least-squares fit of the simulation data. The solid markers in figure 14(a) show the profiles of $f\,(\eta)$ using $A_u = 79.5$ (circles) and 99 (triangles). These values are comparable to the values of 76.5 and 90.2 reported by Xu & Antonia (2002) for jets from a smooth contraction and pipe nozzle, respectively.

Radial profiles of $u'_{\rm rms}/U_c$ from Cases 1 and 1T are compared in figure 14(b). $u'_{\rm rms}/U_c$ attains self-similarity around $x/D \approx 25$, a location which is further downstream than for $\overline{u}/U_c$, in both Cases 1 and 1T; minor differences remain near the centerline between the profiles at $x/D \approx 25$ and 30. $u'_{\rm rms}/U_c$ values from Case 1T are smaller than those from Case 1 at all shown axial locations, especially away from the centerline, consistent with the experimental observations of Xu & Antonia (2002) with laminar/turbulent inflow. Figure 14(b) also shows that for Case 1, $u'_{\rm rms}/U_c$ in the near field ($x/D \approx 15$; shown as solid blue line) is larger than that in the self-similar regime, especially in the radial vicinity of the centerline, while for Case 1T, the near field ($x/D \approx 15$; shown as dashed blue line) values are smaller than that in the self-similar regime. $u'_{\rm rms}/U_c$ values in the near field are, therefore, considerably larger with laminar inflow than with turbulent inflow.

The radial variation of $u'_{\rm rms}\ /u'_{c,{\rm rms}}$ where $u'_{c,{\rm rms}}(x) \equiv u'_{\rm rms}\,(x, r = 0)$, is plotted in

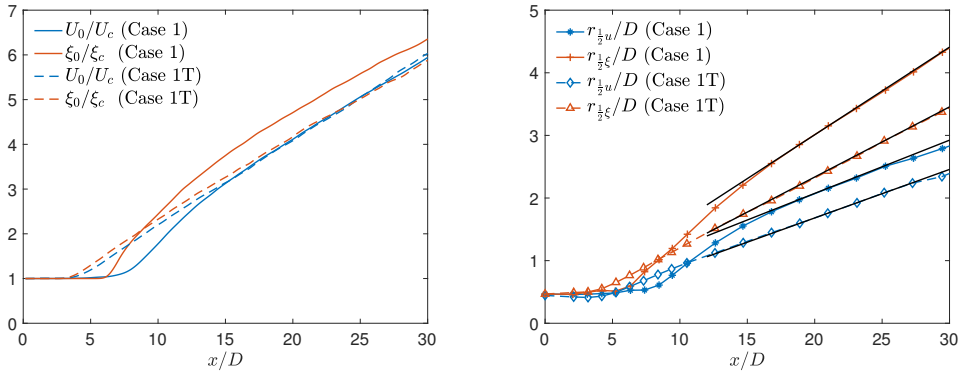

FIGURE 13. Case 1 and 1T comparisons: Streamwise variation of the (a) inverse of centerline mean axial-velocity (U_c) and scalar concentration (ξ_c) normalized by the jet-exit centerline mean values and (b) normalized velocity and scalar half radius, denoted by $r_{\frac{1}{2}u}/D$ and $r_{\frac{1}{2}\xi}/D$, respectively. The black solid lines in subfigure (b) are given by (4.17*a*)–(4.17*d*).

figure 14(c). $u'_{\rm rms}/u'_{c,\rm rms}$ attains self-similarity around $x/D \approx 25$ in Case 1 and as near-stream as $x/D \approx 15$ in Case 1T. Although self-similarity occurs further downstream for Case 1 compared to Case 1T, in the self-similar regime, the maximum value of $u'_{\rm rms}/u'_{c,\rm rms}$ is approximately the same for both cases. With increase in η from the maximum, the decay is steeper in Case 1T, resulting in larger $u'_{\rm rms}/u'_{c,\rm rms}$ in Case 1 at large η. The normalized Reynolds stress, $\overline{u'v'}/U_c^2$, shown in figure 14(d), attains self-similarity around $x/D \approx 25$ for both Cases 1 and 1T. Similar to $u'_{\rm rms}/U_c$, the magnitude of $\overline{u'v'}/U_c^2$ in the self-similar regime is smaller for Case 1T than Case 1, where differences increase with increase in η. In this respect, the behavior of normalized r.m.s. radial and azimuthal velocity fluctuations (not shown here) are similar to that of $u'_{\rm rms}/U_c$ and $\overline{u'v'}/U_c^2$. Thus, although self-similarity is attained by all Reynolds stress components, the self-similar profile depends on the inflow condition.

Examining the passive scalar field, the radial variation of $\bar{\xi}/\xi_c$ and $\xi'_{\rm rms}/\xi'_{c,\rm rms}$ from Cases 1 and 1T are compared in figures 15(a) and (b), respectively. Minor differences between the mean profiles at $x/D \approx 25$ and 30 in figure 15(a) for both cases suggest that the mean scalar field is not fully self-similar, but close to self-similarity at $x/D \approx 30$. The solid markers in figure 15(a) show the profiles of $g(\eta)$, given by (4.19), for $A_\xi = 46.8$ (circles) and 56.2 (triangles), and these values provide a least-squares fit to the mean profile at $x/D \approx 30$ from Cases 1 and 1T, respectively. These values of A_ξ show a similar trend as that observed in the passive scalar measurements of Mi *et al.* (2001) for jets from a smooth contraction ($A_\xi = 56.8$) and a pipe ($A_\xi = 63.3$) nozzle. The $\overline{u}/U_c$ and $\bar{\xi}/\xi_c$ profiles in figures 14(a) and 15(a), respectively, show that both quantities exhibit a steeper decay with η for Case 1T.

The r.m.s. scalar fluctuations, $\xi'_{\rm rms}$, depicted in figure 15(b), increase with radial distance in the vicinity of centerline. The maximum of $\xi'_{\rm rms}/\xi'_{c,\rm rms}$ occurs at larger η than the maximum of $u'_{\rm rms}/u'_{c,\rm rms}$ in figure 14(c). Beyond the maximum, both the velocity and scalar fluctuations decline with increase in η. The decline occurs at a faster rate in Case 1T than in Case 1, resulting in smaller $\xi'_{\rm rms}/\xi'_{c,\rm rms}$ in Case 1T for $\eta \gtrsim 0.1$. For both cases, the profiles at $x/D \approx 25$ and 30 in figure 15(b) differ only marginally, indicating that $\xi'_{\rm rms}/\xi'_{c,\rm rms}$ is nearly self-similar.

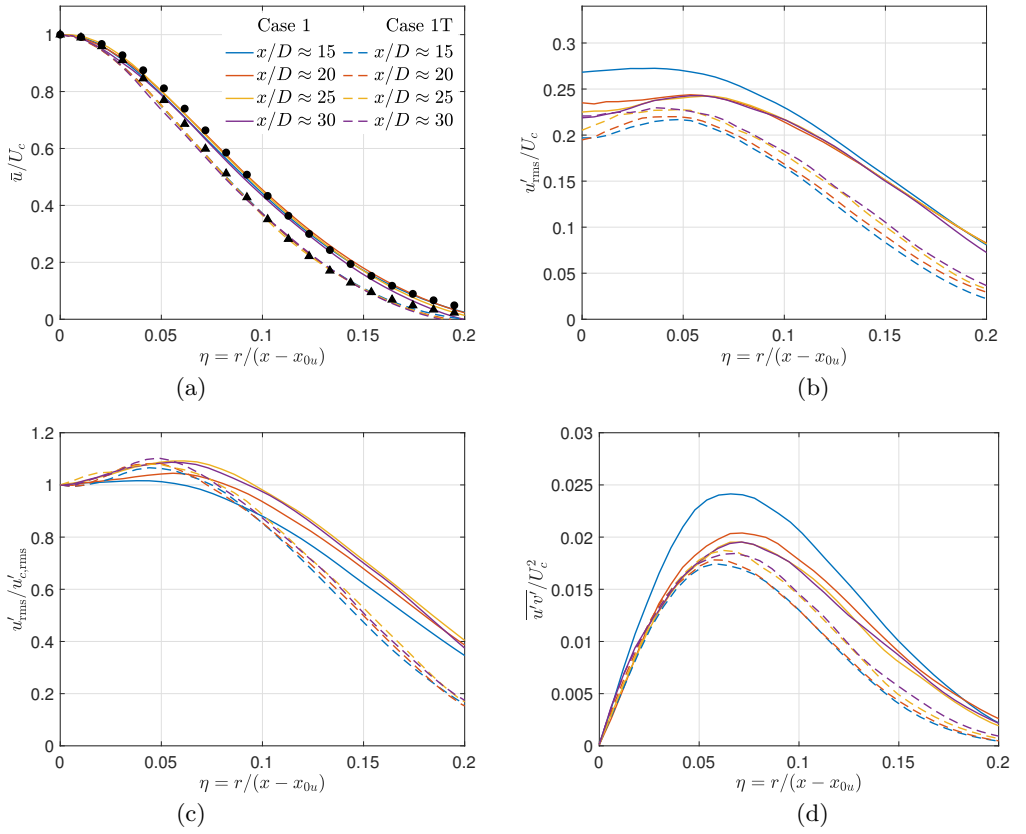

FIGURE 14. Case 1 and 1T comparisons: Radial profiles of (a) mean axial velocity ($\bar{u}$) and (b) r.m.s. axial velocity fluctuations ($u'_{\rm rms}$) normalized by the centerline mean velocity (U_c), (c) r.m.s. axial velocity fluctuations ($u'_{\rm rms}$) normalized by the centerline r.m.s. axial velocity fluctuations ($u'_{c,\rm rms}$), and (d) normalized Reynolds stress ($\overline{u'v'}$) at various axial locations. The markers • and ▲ in subfigure (a) show $f(\eta)$ of (4.19) using $A_u = 79.5$ and 99, respectively. The legend is the same for all plots.

4.2.2.2 Passive scalar mixing

To examine scalar mixing, figure 16 compares the one-point scalar probability density function (p.d.f.) at various locations along the jet centerline between Case 1 and 1T. The p.d.f., $\mathcal{P}(\xi)$, is defined such that

$$\int_0^1 \mathcal{P}\left(\tilde{\xi}\right) \mathrm{d}\tilde{\xi} = 1 \qquad \text{and} \qquad \bar{\xi} = \int_0^1 \tilde{\xi}\mathcal{P}\left(\tilde{\xi}\right) \mathrm{d}\tilde{\xi}. \tag{4.20}$$

Significant differences are observed in the near-field p.d.f. profiles of Cases 1 and 1T in figure 16, *i.e.* for $x/D \lesssim 15$. The locations $x/D \approx 5$ and 8 are approximately the centerline location of maximum (non-dimensionalized) scalar fluctuations for Case 1T and Case 1, respectively, as shown in figure 17. Since the jet-exit centerline mean scalar value is $\xi_0 = 1$ for all cases, normalization of $\xi'_{c,\rm rms}$ with ξ_0 in figure 17 allows a comparison of the absolute fluctuation magnitude between Case 1 and Case 1T. $\xi'_{c,\rm rms}/\xi_0$ peaks when the potential core closes and, then, decreases with axial distance for each case. In contrast,

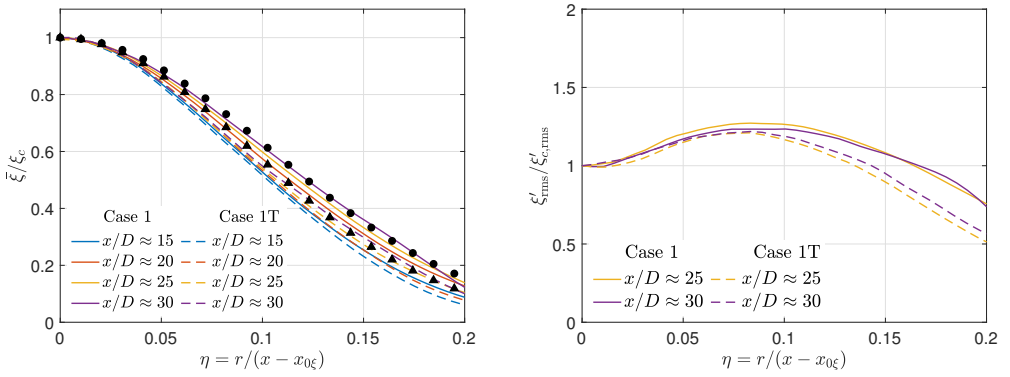

(a) (b)

FIGURE 15. Case 1 and 1T comparisons: Radial profiles of (a) mean scalar concentration ($\bar{\xi}$) normalized by the centerline mean scalar value (ξ_c) and (b) scalar fluctuations ($\xi'_{\rm rms}$) normalized by the centerline r.m.s. scalar fluctuation ($\xi'_{c,\rm rms}$) at various axial locations. The markers • and ▲ in subfigure (a) show $g(\eta)$ of (4.19) using $A_\xi = 46.8$ and 56.2, respectively.

the local normalization with ξ_c asymptotes to a constant value at large axial distances. $\xi'_{c,\rm rms}/\xi_c$ exhibits a prominent hump, or a local maximum, in the near field for Case 1, consistent with the experimental observations in jets from a smooth contraction nozzle (Mi *et al.* 2001).

Comparison of p.d.f. profiles at $x/D \approx 5$ in figure 16 between Case 1 and 1T shows pure jet fluid ($\xi = 1$) for Case 1, whereas mixed fluid with scalar concentrations ranging from 0.5 to 1 for Case 1T, as expected, since the potential core closes before $x/D \approx 5$ in Case 1T, but after $x/D \approx 5$ in Case 1. At $x/D \approx 8$ and 10, the p.d.f. profiles for Case 1 exhibit a wider spread compared to that for Case 1T. Stronger large-scale vortical structures in the near field (around $x/D \approx 8$) in Case 1, as seen in figure 12(a), entrain ambient fluid deep into the jet core resulting in larger scalar fluctuations (see figure 17) and a wider distribution of scalar concentrations at the centerline. In contrast, mixing in Case 1T occurs through small-scale structures resulting in weaker entrainment of ambient fluid and smaller scalar fluctuations. P.d.f. profiles for Case 1T at $x/D \approx 8$ and 10 are, therefore, narrower with higher peaks. Larger scalar fluctuations in the transition region ($7 \lesssim x/D \lesssim 15$) of Case 1, resulting from large-scale organized structures, cause greater mixing and, consequently, steeper decay of the centerline mean scalar concentration (ξ_c), as observed in figure 13(a). The centerline mean scalar concentration, indicated by the scalar value at peaks of the p.d.f. profiles in figure 16, is smaller (or closer to the ambient scalar value of 0) for Case 1 downstream of $x/D \approx 10$. The difference between the scalar mean values from the two cases diminishes with axial distance. With increase in axial distance, the jet-width (see figure 13(b)) increases and the absolute centerline scalar fluctuation (see figure 17) diminishes, and as a result the spread of the scalar p.d.f. profile declines and the peaks become sharper downstream of $x/D \approx 10$.

4.2.2.3 Summary

To conclude, the governing equations for atmospheric-p jets and the numerical method used to solve them quantitatively capture the experimentally documented differences between jets from a smooth converging nozzle and from a pipe, and provide confidence that the simulation setup is correct. This fact combined with the accuracy of the PR EOS and transport properties demonstrated in §4.1, encourage the undertaking of the high-

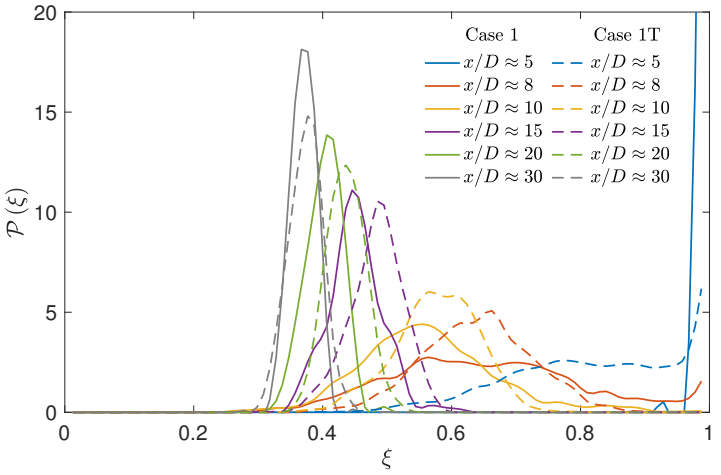

FIGURE 16. Case 1 and 1T comparisons: Scalar probability density function, $\mathcal{P}(\xi)$, at various centerline axial locations.

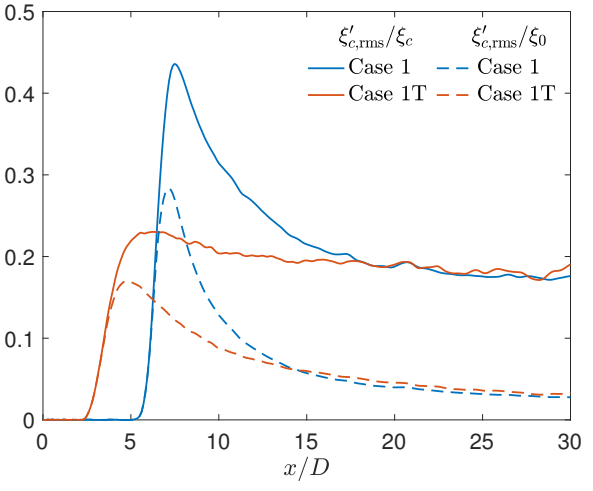

FIGURE 17. Case 1 and 1T comparisons: Streamwise variation of the centerline r.m.s. scalar fluctuation ($\xi'_{c,\mathrm{rms}}$) normalized by the centerline mean scalar value (ξ_c) and the jet-exit centerline mean scalar value (ξ_0).

p jet simulations. Moreover, the present results show that the quantitative knowledge of experimental inflow conditions is necessary in validating simulation results against experiments.

4.3. *Effects of high pressure and compressibility factor*

The influence of p_∞ (from atmospheric to supercritical) on jet-flow dynamics and mixing is here examined by comparing results from Cases 1 and 2. Further, the effects of Z at supercritical p_∞ are examined by comparing results from Cases 2 to 4. As indicated in table 2, in each case the fluid in the injected jet is as dense as the ambient (or chamber) fluid. The inflow bulk velocity, defined by (3.11), is the same for all cases. As a result, the inflow bulk momentum varies with change in inflow density.

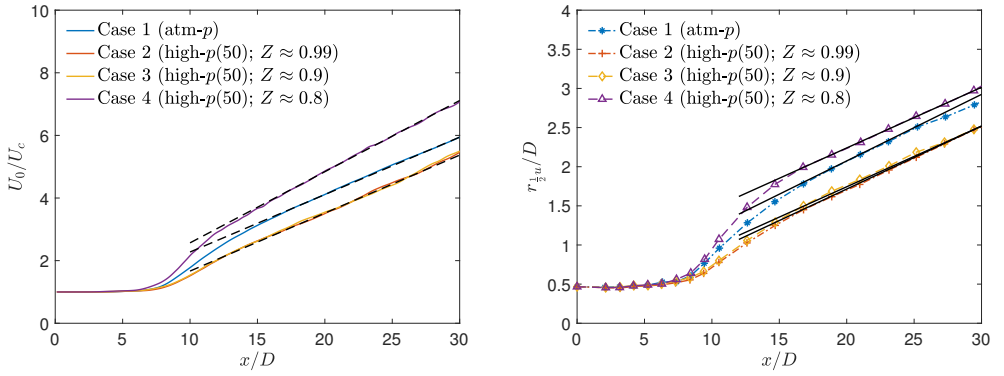

FIGURE 18. Case 1–4 comparisons: Streamwise variation of the (a) inverse of centerline mean axial velocity (U_c) normalized by the jet-exit centerline velocity (U_0) and (b) velocity half radius ($r_{\frac{1}{2}u}$). The black dashed lines in subfigure (a) are given by (4.13) using $B_u = 5.5$, $x_{0u} = -2.4D$ for Case 1, $B_u = 5.4$, $x_{0u} = D$ for Cases 2 & 3, and $B_u = 4.4$, $x_{0u} = -1.3D$ for Case 4. The black solid lines in subfigure (b) are given by (4.17a) and (4.21a)–(4.21c) for respective cases.

4.3.1. *Mean axial velocity and spreading rate*

The inverse of the normalized centerline mean axial-velocity, $(U_c/U_0)^{-1}$, for Cases 1 to 4 is presented in figure 18(a). To our knowledge, figure 18(a) demonstrates for the first time that supercritical jets in the Mach number range [0.58, 0.82], see table 2, attain self-similarity. This finding differs from the self-similarity observed in the low-Mach-number results of Ries *et al.* (2017), where the compressibility effects were ignored and the conservation equations did not use the pressure calculated from the EOS. In contrast, the fully compressible equations solved in the present study use the strongly non-linear EOS which contributes to the thermodynamic-variable fluctuations, and self-similarity is not an obvious outcome.

In figure 18(a), the potential core length is approximately the same in all cases, but the velocity decay rates differ among cases in both the transition and the fully-developed self-similar regions. In the transition region ($7 \lesssim x/D \lesssim 15$), the mean axial-velocity decay, assessed by the slope of the lines in figure 18(a), decreases with increasing p_∞ from 1 bar (Case 1) to 50 bar (Case 2), remains approximately the same with decrease in Z from 0.99 (Case 2) to 0.9 (Case 3), and increases significantly with further decrease in Z to 0.8 (Case 4). In the self-similar region, the decay rates are quantified by the inverse of B_u in (4.13). $1/B_u$ increases from 1/5.5 for Case 1 to 1/5.4 for Case 2 & 3 and to 1/4.4 for Case 4. Lines with slope $1/B_u$ are shown as black dashed lines in figure 18(a).

Figure 18(b) compares the velocity half-radius ($r_{\frac{1}{2}u}$) among Cases 1–4. In the transition region ($7 \lesssim x/D \lesssim 15$), the jet spread defined by the half-radius is larger for Case 1 than Case 2. The profiles are nearly identical for Cases 2 and 3, and Case 4 shows a significantly larger jet spread than Case 3. In the self-similar region, the linear spread can be described by the black solid lines in figure 18(b), given by

$$\text{Case 2:} \qquad r_{\frac{1}{2}u}/D = 0.0805\,(x/D + 1.3)\,, \tag{4.21a}$$

$$\text{Case 3:} \qquad r_{\frac{1}{2}u}/D = 0.0775\,(x/D + 2.5)\,, \tag{4.21b}$$

$$\text{Case 4:} \qquad r_{\frac{1}{2}u}/D = 0.077\,(x/D + 8.9)\,. \tag{4.21c}$$

The solid line for Case 1 is given by (4.17a). The self-similar spread rate decreases from

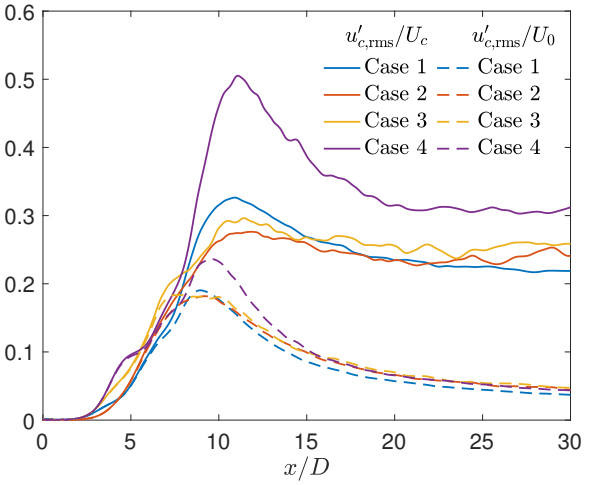

FIGURE 19. Case 1–4 comparisons: Streamwise variation of the centerline r.m.s. axial-velocity fluctuation ($u'_{c,\mathrm{rms}}$) normalized by the centerline mean value, U_c, and jet-exit mean value, U_0.

Case 1 to Case 4. The decrease is relatively small from Case 2 to Case 3, and negligible from Case 3 to Case 4. Variation of ξ_c/ξ_0 and $r_{\frac{1}{2}\xi}/D$ (not shown here for brevity) are similar to those of the velocity field in figure 18.

The decay of U_c, observed in figure 18(a), is a result of the concurrent processes of: (a) transfer of kinetic energy from the mean field to fluctuations, (b) transport of mean kinetic energy away from the centerline as more ambient fluid is entrained, and (c) mean viscous dissipation. These processes interact as follows. The entrainment of ambient fluid (initially at rest) into the jet enhances the momentum and kinetic energy of the ambient fluid. Transport of momentum/energy from the jet core contributes to ambient-fluid entrainment and jet spread. Hence, a wider jet is often associated with larger decay in U_c. Therefore, the variations across cases look similar in figures 18(a) and (b). The variation of U_c across cases in figure 18(a) also follows the variation of t.k.e. production and mean strain rate magnitude, as further discussed in §5. The t.k.e. production term quantifies the loss of mean kinetic energy to turbulent fluctuations and the mean strain rate magnitude is proportional to the mean viscous dissipation.

4.3.2. *Velocity fluctuations and self-similarity*

The mean-kinetic-energy transfer to fluctuations in various cases can be assessed from the centerline r.m.s. axial-velocity fluctuation, depicted in figure 19 for Cases 1–4 with two different normalizations. Since U_0 has the same value for Cases 1–4, the normalization with U_0 compares the absolute fluctuation magnitude among various cases. The normalization with U_c shows the fluctuation magnitude with respect to the local mean value. Larger $u'_{c,\mathrm{rms}}/U_c$ indicates greater local transfer of mean kinetic energy to fluctuations. Accordingly, larger $u'_{c,\mathrm{rms}}/U_c$ in figure 19 implies a higher slope (U_c decay rate) in the corresponding region in figure 18(a). Case 4, which has the largest $u'_{c,\mathrm{rms}}/U_c$ among all cases in both the transition and the self-similar region, also exhibits largest slopes (decay rates) in figure 18(a). Case 1 has larger $u'_{c,\mathrm{rms}}/U_c$ than Cases 2 and 3 in the transition region, and, accordingly, higher decay rates in that region in figure 18(a). In the self-similar region, $u'_{c,\mathrm{rms}}/U_c$ in Cases 2 and 3 are marginally larger than in Case 1,

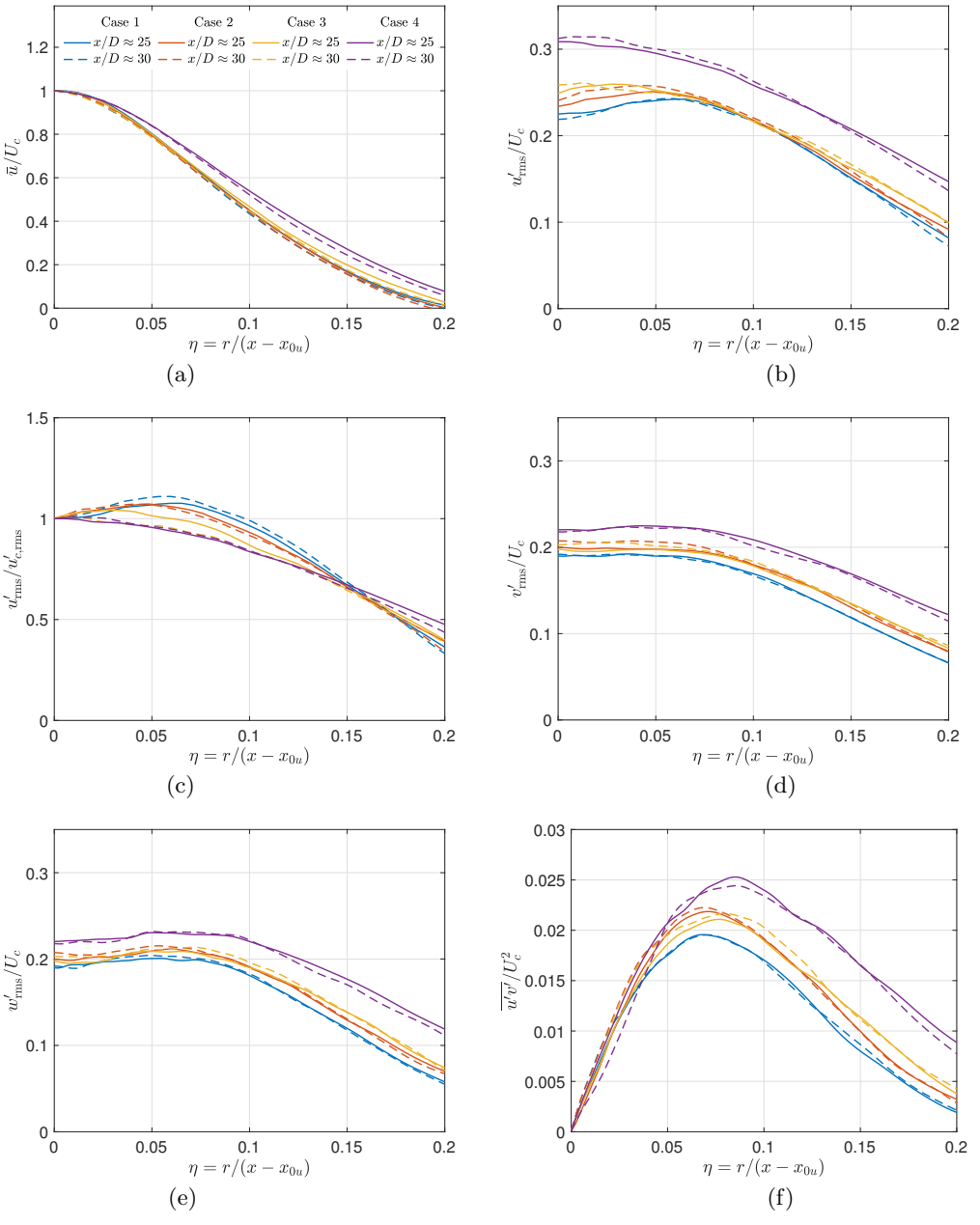

FIGURE 20. Case 1–4 comparisons: Radial profiles of (a) mean axial velocity ($\bar{u}$) normalized by the centerline mean axial velocity (U_c), (b) r.m.s. axial velocity fluctuations ($u'_{\rm rms}$) normalized by the centerline mean axial velocity, (c) r.m.s. axial velocity fluctuations ($u'_{\rm rms}$) normalized by the centerline r.m.s. axial velocity fluctuations ($u'_{c,\rm rms}$), (d) normalized r.m.s. radial velocity fluctuations ($v'_{\rm rms}$), (e) normalized r.m.s. azimuthal velocity fluctuations ($w'_{\rm rms}$), and (f) normalized Reynolds stress ($\overline{u'v'}$) at various axial locations. The legend is the same for all plots.

and hence the self-similar mean-axial-velocity decay rates of Cases 2 and 3 are marginally higher.

The linear mean axial-velocity decay and the linear jet-spread rate, downstream of the transition region, in figure 18 indicates the self-similarity of the mean axial velocity. The self-similarity of mean axial velocity and Reynolds stresses is further examined in figure 20. Figure 20(a) shows the radial profiles of $\bar{u}/U_c$ from Cases 1–4 at $x/D \approx 25$ (solid lines) and 30 (dashed lines). In all cases, profiles at the two axial locations show minimal differences, suggesting that $\bar{u}/U_c$ has attained self-similarity. A least-squares fit of the Gaussian distribution, $f(\eta)$ of (4.19), to $x/D \approx 30$ profiles yields $A_u = 79.5$ for Cases 1 and 2, $A_u = 77.2$ for Case 3, and $A_u = 64.4$ for Case 4. Thus, increasing p from 1 bar (Case 1) to 50 bar (Case 2) has minimal influence on the radial variation of the self-similar axial-velocity profile. A decrease in Z from 0.99 (Case 2) to 0.9 (Case 3) and then to 0.8 (Case 4) at $p_\infty = 50$ bar increases $\bar{u}/U_c$ at a fixed η.

The radial variation of normalized r.m.s. velocity fluctuations at $x/D \approx 25$ and 30 are compared for Cases 1–4 in figures 20(b)–(e). In all figures, the profiles at $x/D \approx 25$ (solid lines) and 30 (dashed lines) show minimal difference, and hence the r.m.s. velocity fluctuations can be considered self-similar around $x/D \approx 25$. $u'_{\rm rms}/U_c$, shown in figure 20(b), increases in the vicinity of centerline with increase in p_∞ from 1 bar (Case 1) to 50 bar (Case 2), but the differences diminish with increase in η. A decrease in Z from 0.99 (Case 2) to 0.9 (Case 3) marginally increases $u'_{\rm rms}/U_c$ at both small and large η. Further decrease in Z from 0.9 (Case 3) to 0.8 (Case 4) shows significant increase in $u'_{\rm rms}/U_c$ at all η-locations. $u'_{\rm rms}/u'_{c,\rm rms}$, plotted in figure 20(c) shows that the fluctuations increase with radial distance near the centerline in Case 1, with maximum at $\eta \approx 0.07$. The location of the maximum (in terms of η) recedes towards the centerline progressively in Cases 2 and 3. Case 4 does not exhibit an off-axis maximum and $u'_{\rm rms}/u'_{c,\rm rms}$ decreases monotonically with η.

$v'_{\rm rms}/U_c$ and $w'_{\rm rms}/U_c$, shown in figures 20(d) and (e), respectively, increase from Case 1 to 4. The increase is marginal from Case 1 to 3, but significant in Case 4. Axisymmetry of a round-jet flow requires that $v'_{\rm rms}$ and $w'_{\rm rms}$ be equal at the centerline, which is nearly true for all cases in figures 20(d) and (e). Comparable profiles of $\overline{u'v'}/U_c^2$ in figure 20(f) at $x/D \approx 25$ and 30 suggest that $\overline{u'v'}/U_c^2$ attains self-similarity around $x/D \approx 25$ in Cases 1–4. $\overline{u'v'}/U_c^2$ is similar for Cases 1–4 in the vicinity of the centerline but the profiles differ at larger η, where Case 4 values are considerably larger than the other cases.

4.3.3. *Pressure and density fluctuations, pressure-velocity correlation, and third-order velocity moments*

The differences in mean axial-velocity for various cases, observed in figure 18, is explained above by the differences in velocity fluctuations. Larger velocity fluctuations imply greater transfer of energy from the mean field to fluctuations, resulting in greater decay of mean velocity. The differences in velocity fluctuations with p_∞ and Z, however, remain to be explained, and this topic is addressed next.

To understand the cause of differences in velocity fluctuations among Cases 1–4 (figures 19 and 20), pressure/density fluctuations, pressure-velocity correlations and third-order velocity moments are examined in figures 21, 22, and 23 because they determine the transport term in the Reynolds stress and t.k.e. equations (e.g. Panchapakesan & Lumley 1993; Hussein *et al.* 1994).

Centerline r.m.s. pressure and density fluctuations normalized using centerline mean values, p_c and ρ_c, respectively, are compared in figure 21(a) for Cases 1–4. The normal-

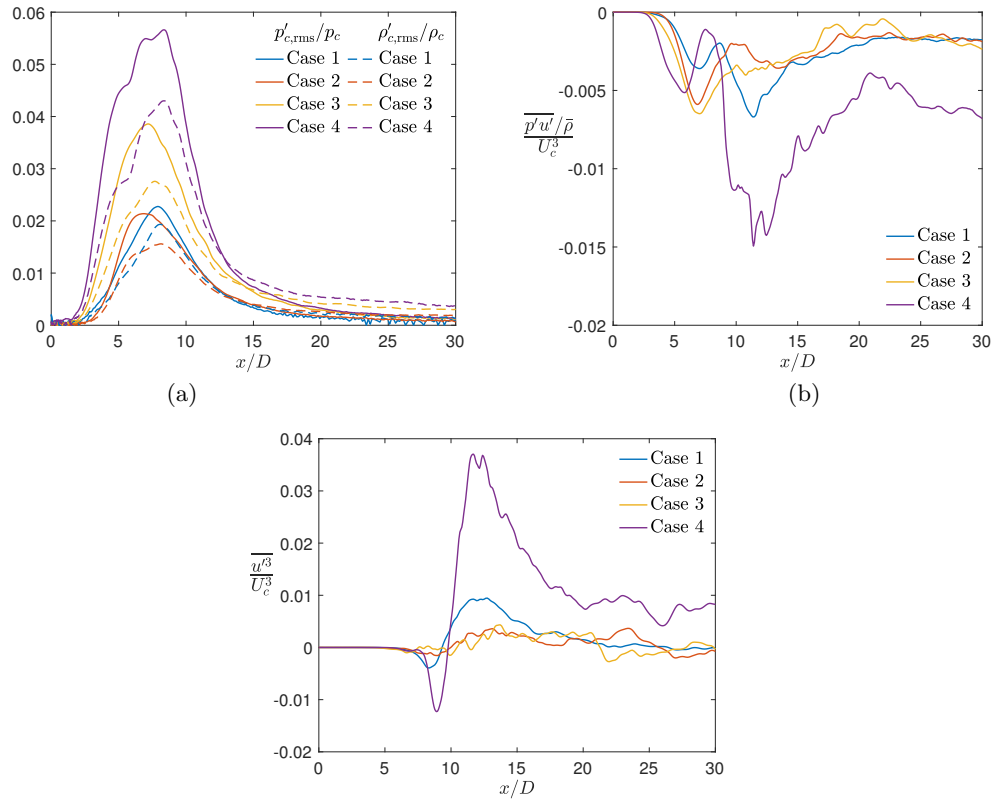

FIGURE 21. Case 1–4 comparisons: Streamwise variation of the (a) centerline r.m.s. pressure and density fluctuations, denoted by $p'_{c,\mathrm{rms}}$ and $\rho'_{c,\mathrm{rms}}$, respectively, normalized by the centerline mean pressure (p_c) and density (ρ_c), respectively, (b) normalized fluctuating pressure-axial velocity correlation $\left(\overline{p'u'}/\bar{\rho}U_c^3\right)$, and (c) normalized third-order velocity moment $\left(\overline{u'^3}/U_c^3\right)$.

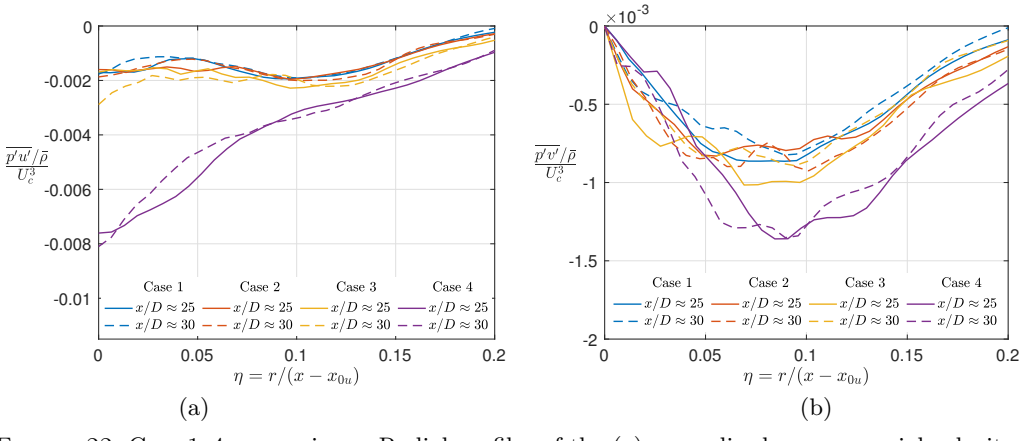

FIGURE 22. Case 1–4 comparisons: Radial profiles of the (a) normalized pressure-axial velocity correlation and (b) normalized pressure-radial velocity correlation at $x/D \approx 25$ and 30.

ization provides information on the fluctuation magnitude with respect to local pressure and density (thermodynamic state). In all cases, $p'_{c,\mathrm{rms}}/p_c$ and $\rho'_{c,\mathrm{rms}}/\rho_c$ have a maximum in the transition region and asymptote to a constant value in the self-similar region. $p'_{c,\mathrm{rms}}/p_c$ exceed $\rho'_{c,\mathrm{rms}}/\rho_c$ in the transition region and vice versa in the self-similar region. Increasing p_∞ from 1 bar (Case 1) to 50 bar (Case 2) slightly reduces $p'_{c,\mathrm{rms}}/p_c$ (shown as solid lines) and $\rho'_{c,\mathrm{rms}}/\rho_c$ (shown as dashed lines) at all centerline locations, whereas decreasing Z from 0.99 (Case 2) to 0.9 (Case 3) and then to 0.8 (Case 4) increases $p'_{c,\mathrm{rms}}/p_c$ and $\rho'_{c,\mathrm{rms}}/\rho_c$ significantly.

The centerline variation of fluctuating pressure-axial velocity correlation, $\overline{p'u'}$, whose axial gradient determines t.k.e. diffusion due to pressure fluctuation transport in the t.k.e. equation, is illustrated in figure 21(b) for Cases 1–4. Large local changes in $\overline{p'u'}$ increase the turbulent transport term magnitude in the t.k.e. equation. The $\overline{p'u'}$ values are non-positive at all centerline locations for all cases, implying that a positive pressure fluctuation (higher than the mean) is correlated with negative velocity fluctuation (lower than the mean) and vice versa. $\frac{\overline{p'u'}/\bar{\rho}}{U_c^3}$ profiles in figure 21(b) for all cases have a local minimum in the near field $5 \lesssim x/D \lesssim 9$ and downstream of that minimum, the variations in $\frac{\overline{p'u'}/\bar{\rho}}{U_c^3}$ are noticeably larger in Cases 1 and 4 than in Cases 2 and 3. In the region $9 \lesssim x/D \lesssim 15$, $\frac{\overline{p'u'}/\bar{\rho}}{U_c^3}$ profiles exhibit distinct minima (with large negative values) in Cases 1 and 4, whereas the profiles of Cases 2 and 3 smoothly approach a near-constant value. The larger variation of $\frac{\overline{p'u'}/\bar{\rho}}{U_c^3}$ in this region in Cases 1 and 4 coincides with the larger decay of mean axial-velocity and greater jet spread in figure 18 and higher axial-velocity fluctuations in figure 19 for those cases. On the centerline, the fluctuating pressure-radial velocity correlation, $\overline{p'v'}$, is null.

In addition to gradients of fluctuating pressure-velocity correlation, the gradients of third-order velocity moments contribute to turbulent transport of t.k.e. and thus the centerline variation of $\overline{u'^3}/U_c^3$ is examined in figure 21(c) for Cases 1–4. The increase in p_∞ from 1 bar (Case 1) to 50 bar (Case 2) reduces the overall axial variations of $\overline{u'^3}/U_c^3$, whereas the decrease in Z from 0.99 (Case 2) to 0.9 (Case 3) at 50 bar pressure has minimal influence on $\overline{u'^3}/U_c^3$ behavior. Further decrease of Z to 0.8 (Case 4) significantly enhances variations in $\overline{u'^3}/U_c^3$. Similar to figure 21(b), regions of large variations in $\overline{u'^3}/U_c^3$ concur with the regions of large changes in mean axial-velocity and large velocity fluctuations in figures 18 and 19, respectively.

The radial variation of fluctuating pressure-velocity correlations and third-order velocity moments at $x/D \approx 25$ and 30 from Cases 1–4 is compared in figures 22 and 23, respectively. Both $\frac{\overline{p'u'}/\bar{\rho}}{U_c^3}$ and $\frac{\overline{p'v'}/\bar{\rho}}{U_c^3}$ exhibit negative values at all radial locations. $\frac{\overline{p'u'}/\bar{\rho}}{U_c^3}$ peaks in absolute magnitude at the centerline, whereas the peak of $\frac{\overline{p'v'}/\bar{\rho}}{U_c^3}$ lies off-axis. The absolute magnitude of $\frac{\overline{p'u'}/\bar{\rho}}{U_c^3}$ in Case 4 is significantly larger than in other cases at all radial locations, implying greater normalized t.k.e. diffusion flux due to pressure fluctuation transport by axial-velocity fluctuations. The normalized radial t.k.e. diffusion flux from pressure fluctuation transport, $\frac{\overline{p'v'}/\bar{\rho}}{U_c^3}$, is similar near the centerline for all cases but larger in magnitude in Case 4 for $\eta \gtrsim 0.075$.

The t.k.e. diffusion fluxes due to transport of Reynolds stresses by the fluctuating velocity field is examined in figure 23 through the third-order velocity moments. All non-zero third-order moments from Cases 1–4 together with the experimental profiles from Panchapakesan & Lumley (1993) are shown in the figure; the Panchapakesan & Lumley (1993) experiments measured all third-order moments except $\overline{v'w'^2}$. Aside from the large

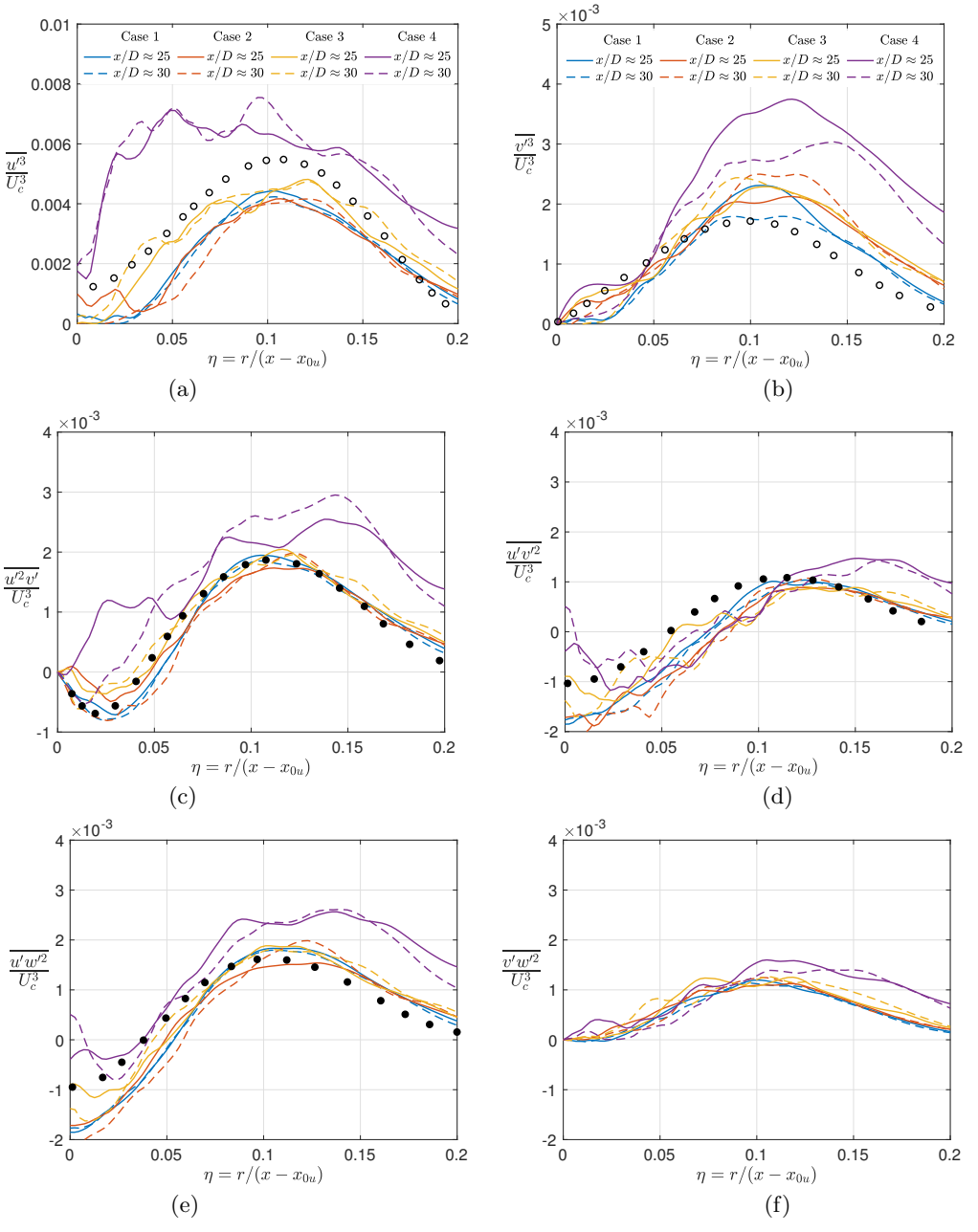

FIGURE 23. Case 1–4 comparisons: Radial profiles of the normalized third-order velocity moments. (a) $\overline{u'^3}/U_c^3$, (b) $\overline{v'^3}/U_c^3$, (c) $\overline{u'^2v'}/U_c^3$, (d) $\overline{u'v'^2}/U_c^3$, (e) $\overline{u'w'^2}/U_c^3$ and (f) $\overline{v'w'^2}/U_c^3$. The black markers • show profiles from the experiments of Panchapakesan & Lumley (1993).

flux values in Case 4, a noticeable feature in correlations $\overline{u'^2v'}$, $\overline{u'v'^2}$ and $\overline{u'w'^2}$ is their negative values near the centerline. The negative $\overline{u'^2v'}$ indicates a radial flux of the axial component of t.k.e., $\overline{u'^2}$, towards the centerline. The smaller region of negative values with decrease in Z from Case 2 to Case 4 indicates a smaller radial flux towards the centerline and a dominant radially outward transport of $\overline{u'^2}$.

4.3.4. *Passive scalar mixing*

Mixing differences among Cases 1–4 is examined in figure 24 using $\mathcal{P}(\xi)$, defined by (4.20), at various centerline locations. Comparisons between Cases 1 and 2, shown in figure 24(a), evaluate the effect of p_∞ increase at approximately same Z value. At $x/D \approx 5$, the centerline contains pure jet fluid ($\xi = 1$) in both cases. The potential core closes downstream of $x/D \approx 5$, and the p.d.f. at $x/D \approx 8$ in both cases shows a wide spread with mixed-fluid concentration in the range $0.3 \lesssim \xi \lesssim 1$. Velocity/pressure statistics in the transition region of Cases 1 and 2 differ significantly, as observed in figures 18, 19 and 21(a). Similarly, $\tilde{\xi}$ and $\xi''_{\rm rms}$ vary in the transition region yielding differences in mixed-fluid composition and $\mathcal{P}(\xi)$. In the transition region, the mean scalar concentration decays at a faster rate in Case 1 than in Case 2, as shown in figure 25(a). As a result, downstream of $x/D \approx 10$, the p.d.f. peaks are closer to the jet pure fluid concentration ($\xi = 1$) in Case 2 than in Case 1. For $x/D \geqslant 10$, the absolute scalar fluctuations $\xi''_{c,\rm rms}/\xi_0$ are larger in Case 2 than in Case 1, despite smaller normalized local fluctuation $\xi''_{c,\rm rms}/\xi_c$ in Case 2, as shown in figure 25(b). Larger $\xi''_{c,\rm rms}/\xi_0$ imply wider p.d.f. profiles with smaller peaks.

Figure 24(b) compares the scalar p.d.f. from Cases 3 and 4 to examine the effect of Z on mixing behavior at supercritical pressure. Analogous to figure 24(a), the p.d.f. profiles at $x/D \approx 5$ and 8 are largely similar between the two cases. Differences in peak scalar value, representing the mean concentration, arise in the transition region, consistent with the observations in figure 25(a). At locations downstream of $x/D \approx 15$, larger $\xi''_{c,\rm rms}/\xi_0$ in Case 3 compared to Case 4 leads to wider p.d.f. profiles with smaller peaks.

4.3.5. *Summary*

The examination of the influence of p_∞ and Z on flow statistics in laminar-inflow jets at fixed Re_D yields several conclusions. The flow exhibits sensitivity to p_∞ and Z in the transition as well as the self-similar region, with larger differences observed in the transition region. Increase in p_∞ from 1 bar (Case 1) to 50 bar (Case 2) reduces $u''_{c,\rm rms}/U_c$, $p''_{c,\rm rms}/p_c$ and $\rho''_{c,\rm rms}/\rho_c$ in the transition region, while the differences are small in the self-similar region. Decrease in Z from 0.99 (Case 2) to 0.9 (Case 3) at $p_\infty = 50$ bar significantly enhances $p''_{c,\rm rms}/p_c$ and $\rho''_{c,\rm rms}/\rho_c$ in both the transition and the self-similar region, whereas the influence on $u''_{c,\rm rms}/U_c$ is minimal. The behavior of $u''_{c,\rm rms}/U_c$ is correlated with the t.k.e. diffusive fluxes, e.g. $\frac{\overline{p'u'}/\bar{\rho}}{U_c^3}$ and $\overline{u'^3}/U_c^3$. Further decrease in Z from 0.9 (Case 3) to 0.8 (Case 4) significantly enhances $u''_{c,\rm rms}/U_c$, $p''_{c,\rm rms}/p_c$ and $\rho''_{c,\rm rms}/\rho_c$ in both the transition and the self-similar region. The decrease in Z also enhances $\xi''_{c,\rm rms}/\xi_c$, leading to greater centerline mixing.

4.4. *Effects of supercritical pressure at a fixed compressibility factor*

The above analysis examined the effects of Z at a fixed supercritical p_∞. Here, we discuss the influence of p_∞ at a fixed Z of 0.9 by comparing results between Cases 3 and 5 (see table 2).

The centerline variation of the mean axial velocity and mean scalar concentration in Cases 3 and 5 is presented in figure 26(a). The differences in the profiles of Cases 3 and 5 are minimal in the transition region and they diminish in the self-similar region. The velocity and scalar half radius showing the jet spread are depicted in figure 26(b). Similar to figure 26(a), minor differences between Cases 3 and 5 are observed in the velocity half-radius ($r_{\frac{1}{2}u}$) in the transition region. In comparison, noticeable differences are observed

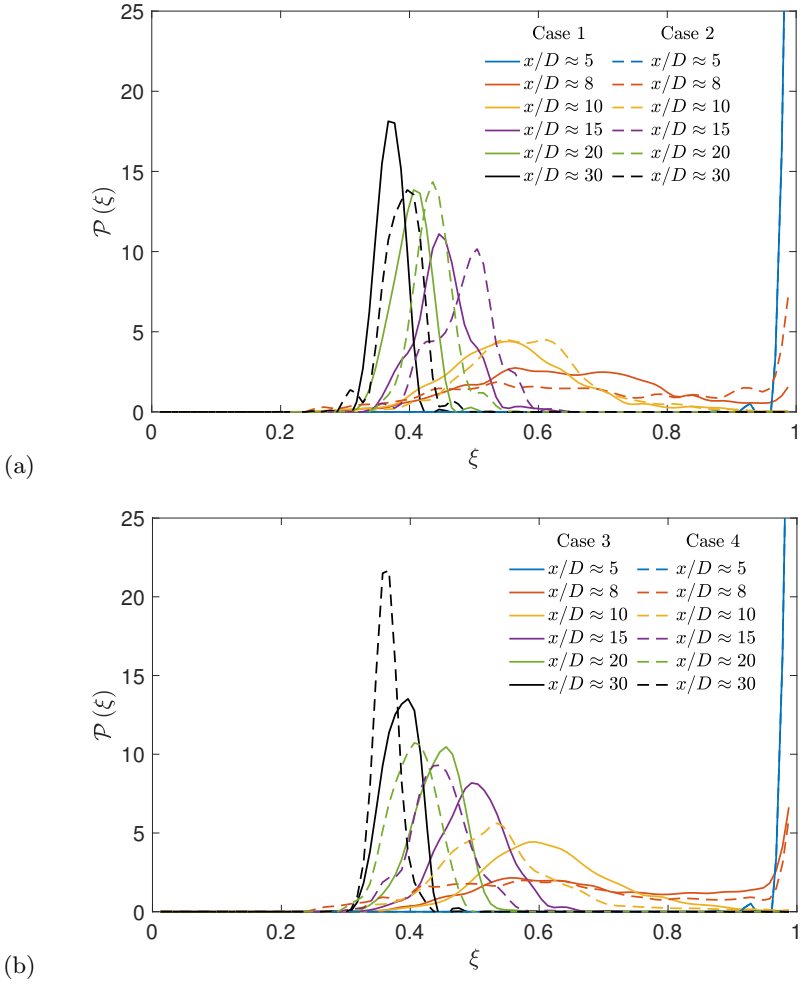

FIGURE 24. Scalar probability density function, $\mathcal{P}(\xi)$, at various centerline axial locations for (a) Cases 1 and 2, and (b) Cases 3 and 4.

in the scalar half-radius ($r_{\frac{1}{2}\xi}$) profiles, where the jet spread in Case 3 is slightly larger than that in Case 5.

To further examine the differences between Case 3 and Case 5, a comparison of the normalized centerline velocity, pressure and density fluctuations is shown in figure 27. Centerline r.m.s. axial-velocity fluctuations with two different normalizations are compared in figure 27(a). U_0 has the same value for Cases 3 and 5, therefore, $u'_{c,\mathrm{rms}}/U_0$ compares the absolute fluctuation magnitude. In contrast, $u'_{c,\mathrm{rms}}/U_c$ depicts the fluctuation magnitude with respect to local mean value. Case 3 exhibits higher $u'_{c,\mathrm{rms}}/U_c$ and $u'_{c,\mathrm{rms}}/U_0$ in the transition region than Case 5. The normalized pressure and density fluctuations, illustrated in figure 27(b), show similar behavior. $p'_{c,\mathrm{rms}}/p_c$ and $\rho'_{c,\mathrm{rms}}/\rho_c$ are larger in Case 3 than Case 5 in the transition region of the flow.

The centerline mixing behavior in Cases 3 and 5 is compared in figure 28 using $\mathcal{P}(\xi)$. While the p.d.f.s at various axial locations look nearly identical, at locations in the transition region and downstream, i.e. $x/D \gtrsim 10$, the p.d.f. peaks are smaller and the

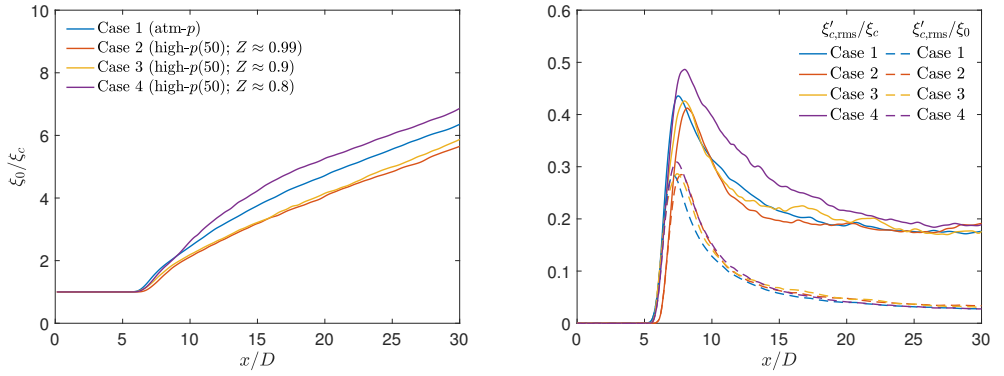

FIGURE 25. Case 1–4 comparisons: Streamwise variation of the (a) inverse of centerline scalar concentration (ξ_c) normalized by the jet-exit centerline value (ξ_0) and (b) centerline r.m.s. scalar fluctuation ($\xi'_{c,\mathrm{rms}}$) normalized by the centerline mean value, ξ_c, and jet-exit mean value, ξ_0.

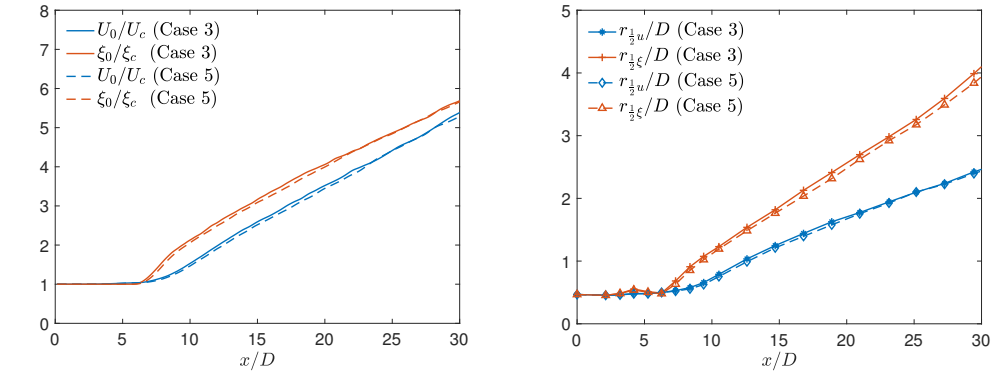

FIGURE 26. Case 3 and 5 comparisons: Streamwise variation of the (a) inverse of centerline mean velocity (U_c) and scalar (ξ_c) normalized by the jet-exit centerline values U_0 and ξ_0, respectively, and (b) velocity and scalar half radius ($r_{\frac{1}{2}u}$ and $r_{\frac{1}{2}\xi}$).

profiles somewhat wider in Case 3, a fact which indicates slightly larger scalar fluctuations and greater mixing than in Case 5.

These results demonstrate that Z does not uniquely determine flow dynamics because Cases 3 and 5 that differ in p_∞ but have same Z exhibit small but noticeable differences in flow fluctuations and mixing. In particular, an increase in supercritical p at a fixed Z leads to a reduced normalized velocity/pressure/density/scalar fluctuations, especially in the transition region. Therefore, the possible notion of performing experiments at a fixed Z and inferring from them information to another state having the same Z (i.e. same departure from perfect-gas behavior) but larger p_∞, where experiments are more challenging, is inadmissible.

4.5. *Inflow effects at high pressure*

A crucial observation from §4.3, where the influence of p_∞ and Z on jet-flow dynamics and mixing was examined, is that $p'_{c,\mathrm{rms}}/p_c$ decreases with increase in p_∞ from 1 bar (Case 1) to 50 bar (Case 2), and increases with decrease in Z from 0.99 (Case 2) to

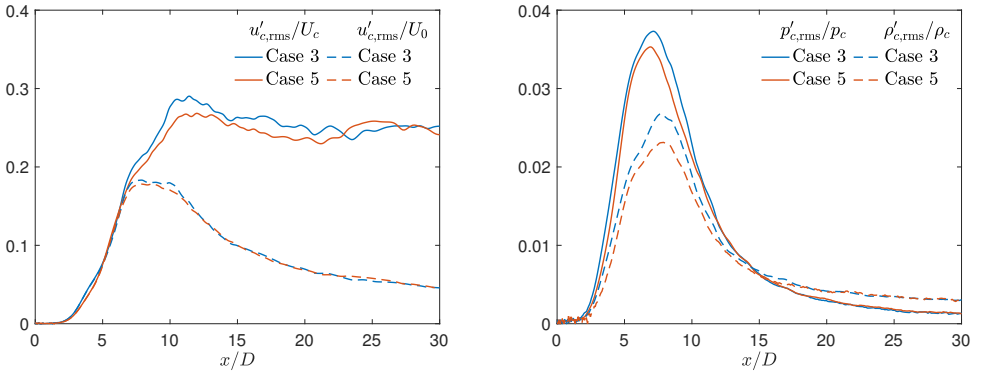

FIGURE 27. Case 3 and 5 comparisons: Streamwise variation of (a) the centerline r.m.s. axial velocity fluctuations ($u'_{c,\mathrm{rms}}$) normalized by the centerline mean axial velocity (U_c) and centerline jet-exit axial velocity (U_0), and (b) the centerline r.m.s. pressure and density fluctuations, denoted by $p'_{c,\mathrm{rms}}$ and $\rho'_{c,\mathrm{rms}}$, respectively, normalized by the centerline mean pressure (p_c) and density (ρ_c), respectively.

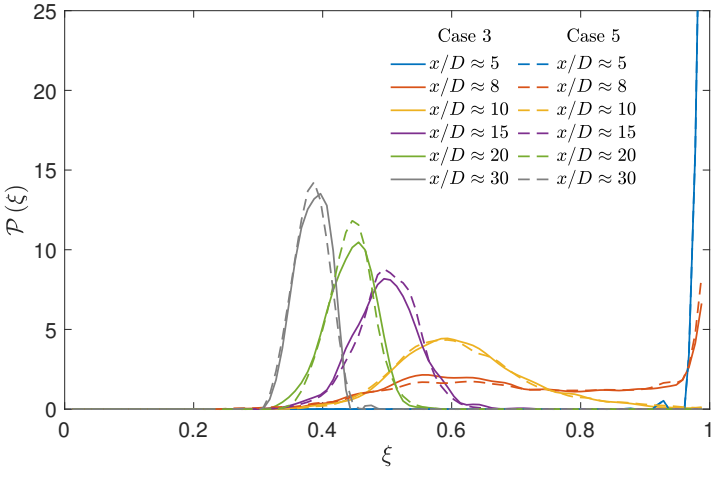

FIGURE 28. Case 3 and 5 comparisons: Scalar probability density function, $\mathcal{P}(\xi)$, at various centerline axial locations.

0.8 (Case 4), as shown in figure 21(a); the velocity/scalar mean and fluctuations (figures 18(a), 19 and 25), however, follow the behavior of the normalized t.k.e. diffusive fluxes (and not of $p'_{c,\mathrm{rms}}/p_c$), e.g. $\frac{\overline{p'u'}/\bar{\rho}}{U_c^3}$ and $\overline{u'^3}/U_c^3$ shown in figures 21(b) and (c), respectively. Those observations are for laminar inflow jets, and the validity of those observations is here examined in pseudo-turbulent inflow jets (see §3.2.2 for inflow details).

The effects of inflow at $p_\infty = 1$ bar were studied in §4.2.2 by comparing results from Cases 1 and 1T. To examine the effects of inflow variation at supercritical p_∞, Case 2 results are here compared with Case 2T, and Case 4 with Case 4T.

4.5.1. *Mean axial velocity and spreading rate*

Figure 29(a) illustrates the centerline variation of mean axial velocity in Cases 1/1T, 2/2T and 4/4T. In concurrence with the observation for Case 1T against Case 1, discussed

in §4.2.2, the pseudo-turbulent inflow cases at supercritical pressure (Cases 2T and 4T) also exhibit a shorter potential core than their laminar inflow counterparts (Cases 2 and 4). As a result, the axial location where the mean velocity decay begins for Cases 1T, 2T and 4T is upstream of the corresponding location for Cases 1, 2 and 4. The laminar inflow cases (solid lines in figure 29(a)) show a distinct transition region ($7 \lesssim x/D \lesssim 15$) with larger mean velocity decay rate than that further downstream in their self-similar region. A similar change in decay rate (equal to the slope of the plot lines) does not occur in Cases 1T, 2T and 4T, where the slopes remain approximately the same downstream of the potential core closure. The linear decay rate in the self-similar region is described by $1/B_u$ in (4.13); larger B_u indicates a smaller decay rate. $B_u = 5.5$ for Cases 1 and 1T, indicating same decay rates in the jets at atmospheric conditions. At $p_{infty} = 50$ bar and $Z = 0.99$, $B_u = 5.4$ for Case 2 and 5.5 for Case 2T, showing slightly larger decay rate for laminar inflow. At $p_{infty} = 50$ bar and $Z = 0.8$, $B_u = 4.4$ for Case 4 and 5.7 for Case 4T, displaying significantly larger decay rate for laminar inflow.

To investigate the differences in jet spread, $r_{\frac{1}{2}u}$ from different inflow cases are compared in figure 29(b). As expected from smaller potential core length in the pseudo-turbulent inflow cases, $r_{\frac{1}{2}u}$ growth in Cases 1T, 2T and 4T begins upstream of that in Cases 1, 2 and 4. Immediately downstream of the potential core closure, $r_{\frac{1}{2}u}$ in laminar inflow cases (Cases 1, 2 and 4) grows at a relatively faster rate than in Cases 1T, 2T and 4T. The linear $r_{\frac{1}{2}u}$ profile in the self-similar region for Cases 1, 2, 4 and 1T are given by (4.17a), (4.21a), (4.21c) and (4.17c), respectively. The profiles for Cases 2T and 4T, shown as dotted lines in figure 29(b), are respectively

$$\text{Case 2T:} \qquad r_{\frac{1}{2}u}/D = 0.079\,(x/D + 2.2)\,, \tag{4.22a}$$

$$\text{Case 4T:} \qquad r_{\frac{1}{2}u}/D = 0.076\,(x/D + 1.3)\,. \tag{4.22b}$$

Thus, the inflow change from laminar to pseudo-turbulent reduces the spreading rate at atmospheric as well as supercritical conditions. The change is significant at atmospheric conditions (from 0.085 in Case 1 to 0.078 in Case 1T) and relatively small for supercritical cases (from 0.0805 in Case 2 to 0.079 in Case 2T and 0.077 in Case 4 to 0.076 in Case 4T). A noticeable feature in the self-similar region of figure 29(b) is the difference in $r_{\frac{1}{2}u}$ among various cases for the two inflows; for laminar inflow, $r_{\frac{1}{2}u}$ decreases from Case 1 to Case 2 and increases from Case 2 to Case 4, whereas the differences are comparatively minimal between Cases 1T, 2T and 4T. In fact, $r_{\frac{1}{2}u}$ in Cases 1T and 2T are slightly larger than that in Case 4T.

4.5.2. *Velocity fluctuations and self-similarity*

To understand the differences observed in figure 29, the centerline variation of axial-velocity fluctuations is compared for various inflow cases in figure 30. $u'_{c,\mathrm{rms}}/U_c$, presented in figure 30(a), reflects the local mean energy transfer to fluctuations. As discussed in §4.3, higher $u'_{c,\mathrm{rms}}/U_c$ implies larger mean axial-velocity decay rate or higher slope of the line in figure 29(a). In the transition region, the laminar inflow cases exhibit significant differences with increase in p_∞ (from Case 1 to Case 2) as well as with decrease in Z (from Case 2 to Case 4). In contrast, the differences are minimal between Cases 1T, 2T and 4T. In the transition region of these cases ($3 \lesssim x/D \lesssim 8$), $u'_{c,\mathrm{rms}}/U_c$ in Case 4T is slightly smaller than that in Cases 1T and 2T. Accordingly, the mean axial-velocity decay rate is smaller for Case 4T in the transition region, see figure 29(a). The difference between the asymptotic value attained by $u'_{c,\mathrm{rms}}/U_c$ is small between Cases 1 and 1T, but significant at supercritical p_∞ between Cases 2 and 2T and Cases 4 and 4T.

Normalizing $u'_{c,\mathrm{rms}}$ with U_0, as presented in figure 30(b), enables a comparison of the

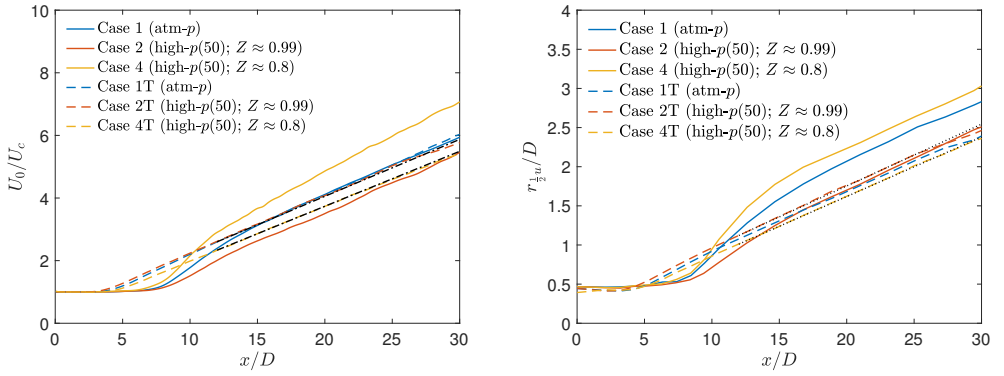

FIGURE 29. Comparisons of different inflow cases: Streamwise variation of the (a) inverse of centerline mean velocity (U_c) normalized by the jet-exit centerline velocity (U_0) and (b) velocity half-radius ($r_{\frac{1}{2}u}$). The black dash-dotted lines in subfigure (a) are given by (4.13) using $B_u = 5.5$, $x_{0u} = -2.3D$ for Case 2T and $B_u = 5.7$, $x_{0u} = -1.3D$ for Case 4T. Lines showing the self-similar profile (4.13) for Cases 1, 2, 4 and 1T are presented in figures 13 and 18. The black dotted lines in subfigure (b) are given by (4.22a) for Case 2T and (4.22b) for Case 4T.

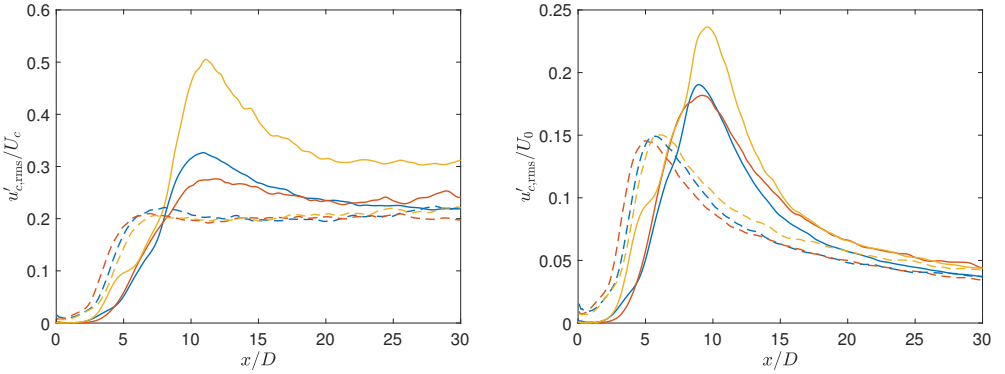

FIGURE 30. Comparisons of different inflow cases: Streamwise variation of the (a) the centerline r.m.s. axial velocity fluctuations ($u'_{c,\mathrm{rms}}$) normalized by the centerline mean axial velocity (U_c), (b) $u'_{c,\mathrm{rms}}$ normalized by the jet-exit centerline mean axial velocity (U_0). The legend is the same for both plots.

absolute fluctuation magnitude for each inflow. U_0 differs for the two inflows, as discussed in §4.2.2. In figure 30(b), $u'_{c,\mathrm{rms}}/U_0$ decreases with axial distance, unlike $u'_{c,\mathrm{rms}}/U_c$ in figure 30(a) that asymptotes to a constant value. The peak of $u'_{c,\mathrm{rms}}/U_0$, attained in the transition region, decreases with increasing p_∞ from 1 bar to 50 bar and increases with decreasing Z from 0.99 to 0.8 for each inflow. The differences between the profiles of pseudo-turbulent inflow cases are small at all axial locations.

The radial variations of mean axial velocity and Reynolds stresses at three axial locations are compared between Cases 2 and 2T and Cases 4 and 4T in figures 31 and 32, respectively. The axial location $x/D \approx 10$ lies around the jet transition region in both inflow cases, whereas the profiles at $x/D \approx 25$ and 30 help assess self-similarity. Figure 31(a) shows that $\bar{u}/U_c$ attains self-similarity upstream of $x/D \approx 25$ in both cases

(2 and 2T); however, the self-similar profile is different as shown by least-squares fits of the Gaussian distribution, $f(\eta)$ of (4.19), to $x/D \approx 30$ profiles, which are depicted as solid markers in figure 31(a): $A_u = 79.5$ (triangles) for Case 2 and $A_u = 99.2$ (circles) for Case 2T.

$u'_{\rm rms}/U_c$ and $u'_{\rm rms}/u'_{c,\rm rms}$ profiles at $x/D \approx 25$ and 30, shown in figures 31(b) and (c), respectively, exhibit only minor differences in both Cases 2 and 2T, suggesting that $u'_{\rm rms}/U_c$ and $u'_{\rm rms}/u'_{c,\rm rms}$ are self-similar around $x/D \approx 25$. $u'_{\rm rms}/U_c$ is considerably larger in the laminar inflow case (Case 2) at all η locations, consistent with the observations at atmospheric p_∞ between Cases 1 and 1T in figure 14(b). Similarly, $\overline{u'v'}/U_c^2$, presented in figure 31(d), also shows larger magnitude in Case 2 for $\eta \gtrsim 0.03$ and self-similarity around $x/D \approx 25$. The normalized r.m.s. radial and azimuthal velocity fluctuations (not shown here for brevity) are also larger in Case 2 than Case 2T.

$\bar{u}/U_c$ from Cases 4 and 4T are compared in figure 32(a). As in figures 14(a) and 31(a) for Cases 1/1T and 2/2T, the self-similar profile are different for the two inflows, and this difference is enhanced with respect to Cases 2/2T as the solid markers in figure 32(a) that display the Gaussian distribution, $f(\eta)$ of (4.19) show: $A_u = 64.4$ (triangles) for Case 4 and $A_u = 99.2$ (circles) for Case 4T. $u'_{\rm rms}/U_c$ and $\overline{u'v'}/U_c^2$, illustrated in figure 32(b) and (d), respectively, show self-similarity around $x/D \approx 25$ for both cases (4 and 4T) and larger magnitude in the laminar inflow case (Case 4). $u'_{\rm rms}/u'_{c,\rm rms}$ in figure 32(c) shows immediate decline with increase in η in Case 4, whereas in Case 4T, it increases slightly in the vicinity of the centerline and then decreases for $\eta \gtrsim 0.05$. The decay rate with η is larger in Case 4T than in Case 4.

4.5.3. *Pressure and density fluctuations, pressure-velocity correlation, and third-order velocity moments*

Centerline variations of $p'_{c,\rm rms}/p_c$ and $\rho'_{c,\rm rms}/\rho_c$ are presented in figures 33(a) and (b), respectively. $p'_{c,\rm rms}/p_c$ and $\rho'_{c,\rm rms}/\rho_c$ are negligible at jet exit in laminar inflow cases but have significant magnitude in pseudo-turbulent inflow cases, where it decreases with axial distance until the potential core closes and increases in the transition region. Variations of $p'_{c,\rm rms}/p_c$ and $\rho'_{c,\rm rms}/\rho_c$ with p_∞ and Z are similar for the two inflows. $p'_{c,\rm rms}/p_c$ and $\rho'_{c,\rm rms}/\rho_c$ are larger in Case 4 than in Cases 1 and 2 and, similarly, they are higher in Case 4T than in Cases 1T and 2T. With increase in p_∞ from 1 bar (Cases 1 and 1T) to 50 bar (Cases 2 and 2T), the peak value of $p'_{c,\rm rms}/p_c$ and $\rho'_{c,\rm rms}/\rho_c$ in the transition region decreases by a small value. The differences diminish downstream in the self-similar region.

$p'_{c,\rm rms}/p_c$ and $\rho'_{c,\rm rms}/\rho_c$ increase with decrease in Z from 0.99 (Cases 2 and 2T) to 0.8 (Cases 4 and 4T) for both inflows, especially in the transition region of the flow. On the other hand, $u'_{c,\rm rms}/U_c$, presented in figure 30(a), increases with decreasing Z for laminar inflow but remains approximately the same in pseudo-turbulent inflow cases. In fact, in the transition region, $u'_{c,\rm rms}/U_c$ is slightly smaller in Case 4T than Case 2T, while it is larger in Case 4 than Case 2. This anomaly with inflow change leads to contrasting mean flow behavior, observed in figure 29 in the transition region, where the mean axial-velocity decay and jet half-radius increases from Case 2 to Case 4 but decreases from Case 2T to Case 4T.

To investigate this anomaly, the centerline variation of t.k.e. diffusion fluxes from turbulent transport is compared in figures 34 and 35. $\frac{\overline{p'u'}/\bar{\rho}}{U_c^3}$, plotted in figure 34, determines t.k.e. diffusion due to pressure fluctuation transport. Figure 34(a) compares $\frac{\overline{p'u'}/\bar{\rho}}{U_c^3}$ from both inflow cases, whereas figure 34(b) shows only the pseudo-turbulent cases

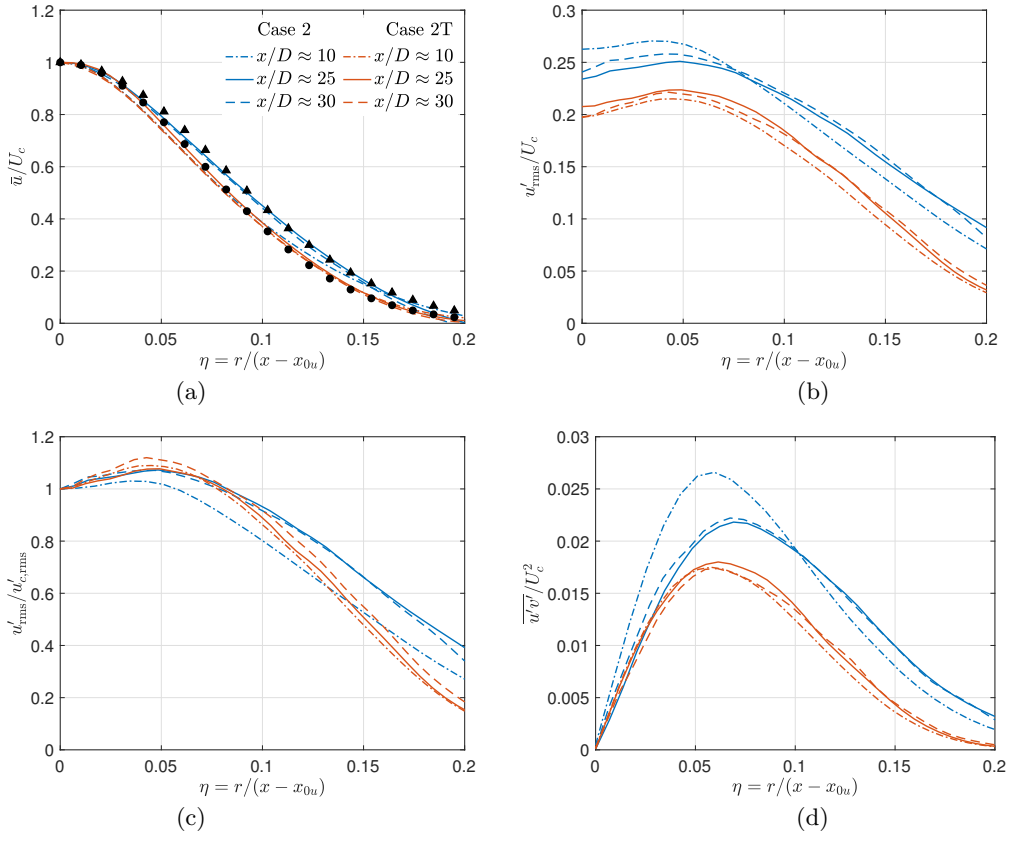

FIGURE 31. Case 2 and 2T comparisons:Radial profiles of (a) mean axial velocity ($\bar{u}$) normalized by the centerline mean axial velocity (U_c), (b) r.m.s. axial-velocity fluctuations ($u'_{\rm rms}$) normalized by the centerline mean axial velocity, (c) r.m.s. axial-velocity fluctuations ($u'_{\rm rms}$) normalized by the centerline r.m.s. axial-velocity fluctuations ($u'_{c,\rm rms}$), and (d) normalized Reynolds stress ($\overline{u'v'}$) at various axial locations. The markers ▲ and • in subfigure (a) show $f(\eta)$ of (4.19) using $A_u = 79.5$ and 99.2, respectively. The legend is the same for all plots.

to highlight differences among them. In the transition region, the absolute magnitude of $\frac{\overline{p'u'}/\bar{\rho}}{U_c^3}$ increases from Case 2 to Case 4, but decreases from Case 2T to 4T. Further downstream, the differences are significant between Case 2 and Case 4, but minimal between Case 2T and 4T. $\overline{u'^3}/U_c^3$, that determines t.k.e. diffusion flux from turbulent transport of $\overline{u'^2}$, is compared between Cases 1/1T, 2/2T and 4/4T in figure 35(a) and among cases 1T/2T/4T in figure 35(b). While there are significant differences in $\overline{u'^3}/U_c^3$ profiles of Cases 1, 2 and 4, the differences are, again, minimal among Cases 1T, 2T and 4T. The variation of t.k.e. diffusion fluxes in figures 34 and 35 for various cases agree with the behavior of $u'_{c,\rm rms}/U_c$ in figure 30(a) and the mean-flow metrics in figure 29.

4.5.4. *Passive scalar mixing*

To examine passive scalar mixing with inflow change at high pressure, the scalar p.d.f. is depicted in figure 36; Cases 2 and 2T are compared at various x/D in figure 36(a) and, similarly, Cases 4 and 4T are compared in figure 36(b). As observed in figure 16 at atmospheric p_∞, the p.d.f. at $x/D \approx 5$ in figure 36(a) shows pure jet fluid in the laminar

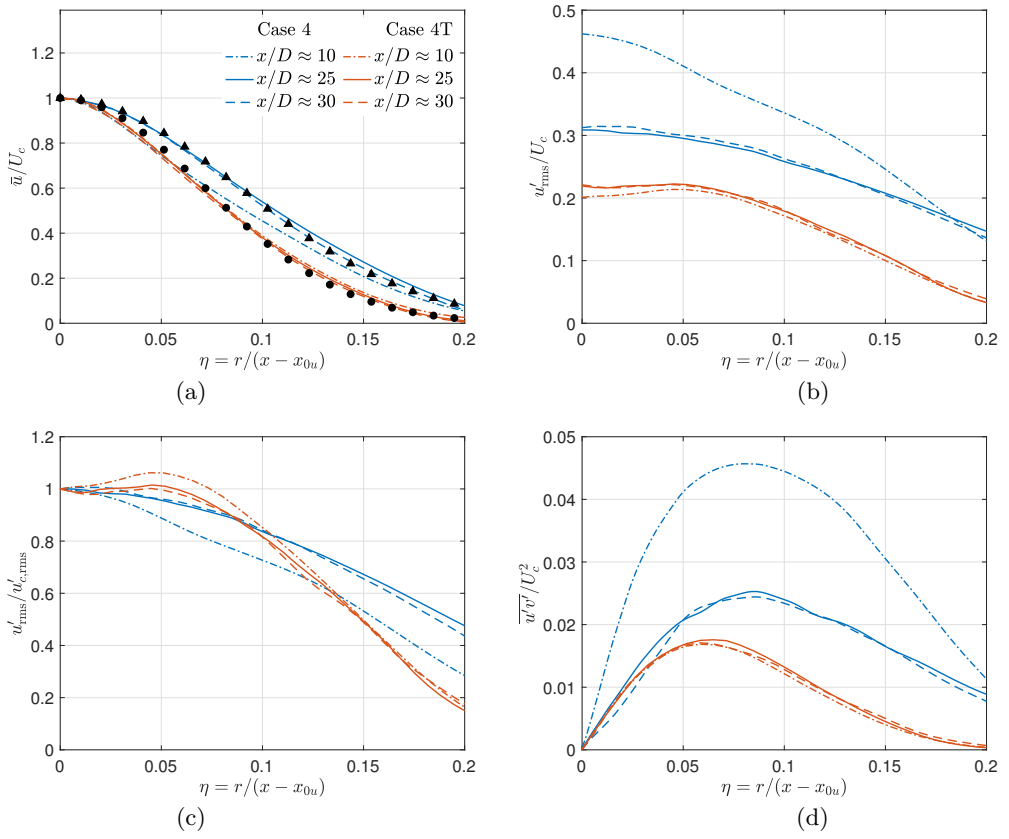

FIGURE 32. Case 4 and 4T comparisons:Radial profiles of (a) mean axial velocity ($\bar{u}$) normalized by the centerline mean axial velocity (U_c), (b) r.m.s. axial-velocity fluctuations ($u'_{\rm rms}$) normalized by the centerline mean axial-velocity, (c) r.m.s. axial-velocity fluctuations ($u'_{\rm rms}$) normalized by the centerline r.m.s. axial-velocity fluctuations ($u'_{c,\rm rms}$), and (d) normalized Reynolds stress ($\overline{u'v'}$) at various axial locations. The markers ▲ and • in subfigure (a) show $f(\eta)$ of (4.19) using $A_u = 64.4$ and 99.2, respectively. The legend is the same for all plots.

inflow case (Case 2), whereas mixed fluid in Case 2T. At $x/D \approx 8$ and 10, the p.d.f. has a wider distribution in Case 2 owing to stronger large-scale vortical structures that yield larger normalized scalar fluctuations, $\xi'_{c,\rm rms}/\xi_0$, as shown in figure 37(b). Further downstream, the p.d.f. profiles show minor differences, consistent with the scalar mean and fluctuation behavior shown in figure 37.

Comparing the p.d.f. from Cases 4 and 4T, the differences in distributions at $x/D \approx 5$ and 8, influenced by the potential core length, are similar to that in figures 16 and 36(a). Significant differences are observed between the downstream p.d.f. profiles (at $x/D \approx 15$, 20 and 30) of Case 4 and Case 4T in figure 36(b), unlike the Cases 2/2T profiles in figure 36(a). The Case 4 p.d.f. peaks are further away from the jet pure fluid concentration ($\xi = 1$) and are larger than in Case 4T. The peaks in a symmetric unimodal p.d.f. coincide with the mean value, therefore, the differences in p.d.f. peak location and magnitude in figure 36(b) mirrors the differences observed in 37(a) between Case 4 and Case 4T.

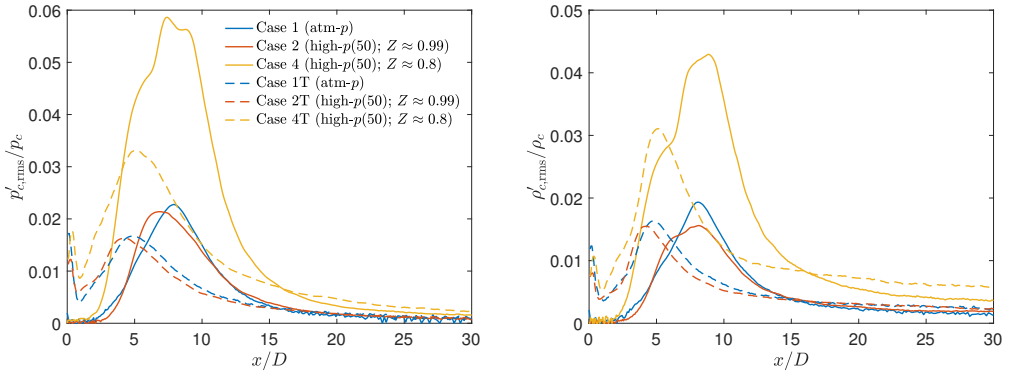

FIGURE 33. Comparisons of different inflow cases: Streamwise variation of the (a) the centerline r.m.s. pressure ($p'_{c,\mathrm{rms}}$) normalized by the centerline mean pressure (p_c) and (b) the centerline r.m.s. density fluctuations ($\rho'_{c,\mathrm{rms}}$) normalized by the centerline mean density (ρ_c). The legend is the same for both plots.

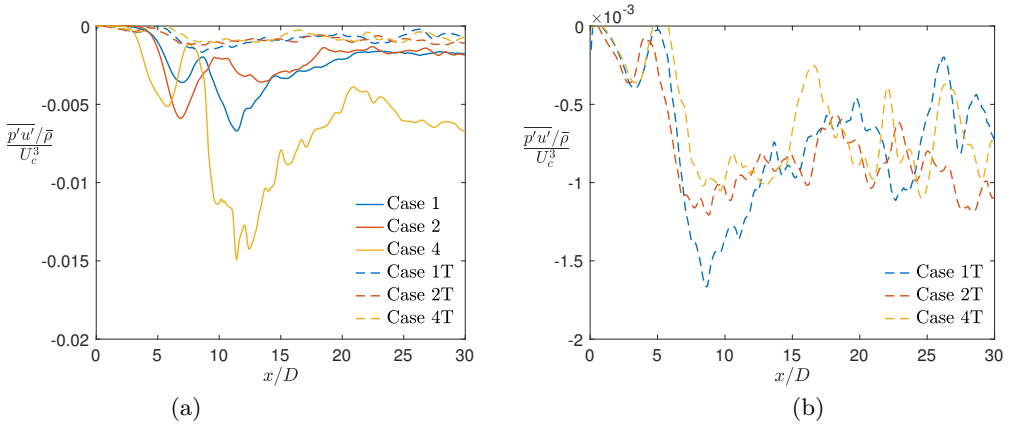

FIGURE 34. Comparisons of different inflow cases: Streamwise variation of the normalized pressure-axial velocity correlation for (a) the laminar and pseudo-turbulent inflow cases, and (b) only the pseudo-turbulent inflow cases. Note the difference between y-axis scales of (a) and (b).

4.5.5. *Summary*

To summarize the above results, the variation of $p'_{c,\mathrm{rms}}/p_c$ and $\rho'_{c,\mathrm{rms}}/\rho_c$ with p_∞ and Z is similar for both inflows, as shown in figures 33(a) and (b). An increase in p_∞ from Case 1/1T to Case 2/2T, at approximately the same Z, reduces $p'_{c,\mathrm{rms}}/p_c$ and $\rho'_{c,\mathrm{rms}}/\rho_c$ marginally, whereas a decrease in Z from Case 2/2T to Case 4/4T increases $p'_{c,\mathrm{rms}}/p_c$ and $\rho'_{c,\mathrm{rms}}/\rho_c$. However, $u'_{c,\mathrm{rms}}/U_c$, shown in figure 30(a), varies differently for the two inflows. A decrease in Z from Case 2 to Case 4 increases $u'_{c,\mathrm{rms}}/U_c$, whereas the same decrease in Z from Case 2T to Case 4T has minimal influence on $u'_{c,\mathrm{rms}}/U_c$. The normalized fluctuating pressure-velocity correlation and third-order velocity moments (that determine t.k.e. diffusion fluxes from turbulent transport) show similar variations as that of $u'_{c,\mathrm{rms}}/U_c$ in each inflow cases. These differences are further discussed next.

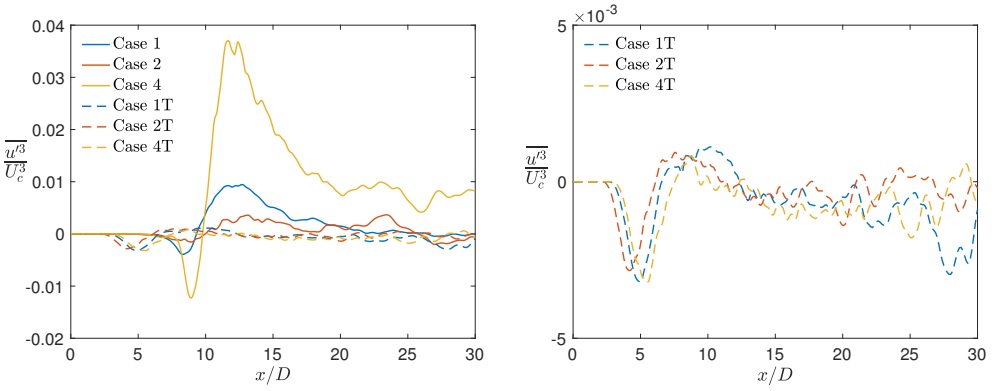

FIGURE 35. Comparisons of different inflow cases: Streamwise variation of $\overline{u'^3}/U_c^3$ for (a) the laminar and pseudo-turbulent inflow cases, and (b) only the pseudo-turbulent inflow cases. Note the difference between y-axis scales of (a) and (b).

5. Discussion

The effect of decreasing Z on $u'_{c,\mathrm{rms}}/U_c$ (which determines centerline scalar fluctuations and turbulent mixing) depends on the inflow, as observed in figure 30(a). In general, the jets from laminar inflow exhibit higher mean strain rates in the transition region than the jets from pseudo-turbulent inflow, as shown in figure 38. The mean strain rate magnitude is defined as

$$\left|\bar{\mathbf{S}}\right| = \left(2\bar{S}_{ij}\bar{S}_{ij}\right)^{1/2}, \tag{5.23}$$

where $\bar{S}_{ij}$ is the mean rate-of-strain tensor. Normalization of $\left|\bar{\mathbf{S}}\right|$ with U_c/D in figure 38(a) illustrates the strain rate magnitude with respect to the local mean field, whereas normalization with U_0/D in figure 38(b) provides absolute strain rate magnitude, since U_0 is the same for all cases of an inflow. The behavior of $\left|\bar{\mathbf{S}}\right|$ in figure 38 agrees well with the behavior of $u'_{c,\mathrm{rms}}$ in figures 30(a) and (b). Normalized $\left|\bar{\mathbf{S}}\right|$ and $u'_{c,\mathrm{rms}}$ results from Case 2T and 4T show minimal difference, unlike $p'_{c,\mathrm{rms}}/p_c$ and $\rho'_{c,\mathrm{rms}}/\rho_c$ results in figures 33(a) and (d), respectively, that are significantly different.

Larger mean strain rates enhance t.k.e. production, as evident from figure 39. The Favre-averaged t.k.e. is defined as $\tilde{k} = \frac{1}{2}\widetilde{u''_i u''_i}$, where tilde ($\tilde{\bullet}$) denotes the Favre average, $\tilde{\phi} = \overline{\rho\phi}/\bar{\rho}$, and $u''_i = u_i - \tilde{u}_i$; $\tilde{k}/U_0^2$ is presented in figure 39(a). The production term of the t.k.e. equation (Huang *et al.* 1995, Equation (3.4)) is

$$P = -\bar{\rho}\widetilde{u''_i u''_j}\frac{\partial \tilde{u}_i}{\partial x_j}, \tag{5.24}$$

and its centerline variation non-dimensionalized using jet-exit values is illustrated in Figure 39(b). Clearly, the variation of Favre-averaged t.k.e. in figure 39(a) for different cases is similar to the variation of the production term magnitude in figure 39(b) and also to the variation of the fluctuating pressure-velocity correlation and the third-order velocity moments (which determine the turbulent transport of t.k.e.) in figures 34 and 35, respectively. This suggests that the changes in p_∞ and Z alter flow dynamics by modifying the structure of turbulence influencing production and transport terms, and not just the compressibility-related dilatational terms, of the t.k.e. equation.

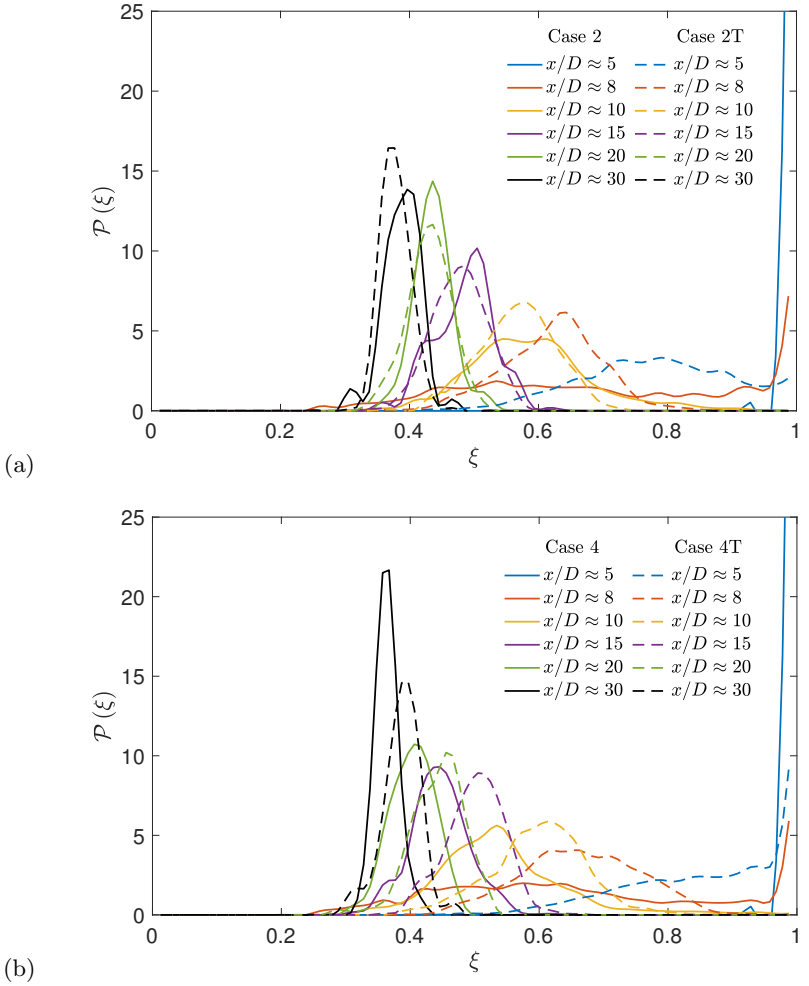

FIGURE 36. Scalar probability density function, $\mathcal{P}(\xi)$, at various centerline axial locations for (a) Cases 2 and 2T, and (b) Cases 4 and 4T.

6. **Conclusions**

Turbulent round-jet DNS at perfect gas (subcritical) and real gas (supercritical) conditions were performed to compare and contrast the effects of pressure (p), compressibility factor (Z) and inflow condition on flow development and turbulence statistics. In all cases, the Reynolds number, Re_D, is 5000. The equation of state and transport coefficient models were chosen to accurately represent the flow conditions. For supercritical pressures, the transport coefficient models were validated with the NIST database. To examine the influence of inflow conditions, a laminar inflow with top-hat velocity profile (and small random perturbations) and a pseudo-turbulent inflow with statistics matching pipe-flow turbulence data were considered.

The self-similar radial profiles of the mean axial velocity and Reynolds stress components from near-atmospheric-p simulation (Case 1) compare well with experimental results (figures 8 and 9). Variations in these profiles and passive-scalar mixing with change in inflow supports the experimental and theoretical result that both near- and far-field flow statistics are influenced by the inflow condition. More specifically, the self-similar

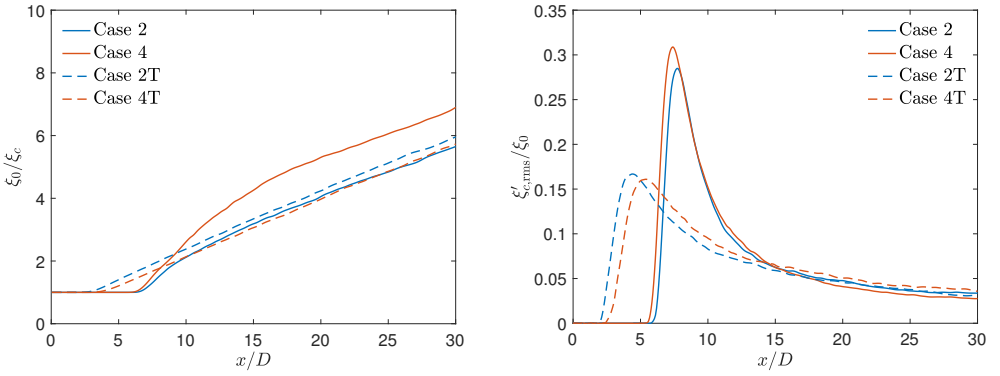

(a) (b)

FIGURE 37. Streamwise variation of the (a) inverse of centerline scalar concentration (ξ_c) normalized by the jet-exit centerline value (ξ_0) and (b) centerline r.m.s. scalar fluctuation ($\xi'_{c,\mathrm{rms}}$) normalized by the centerline jet-exit mean value (ξ_0).

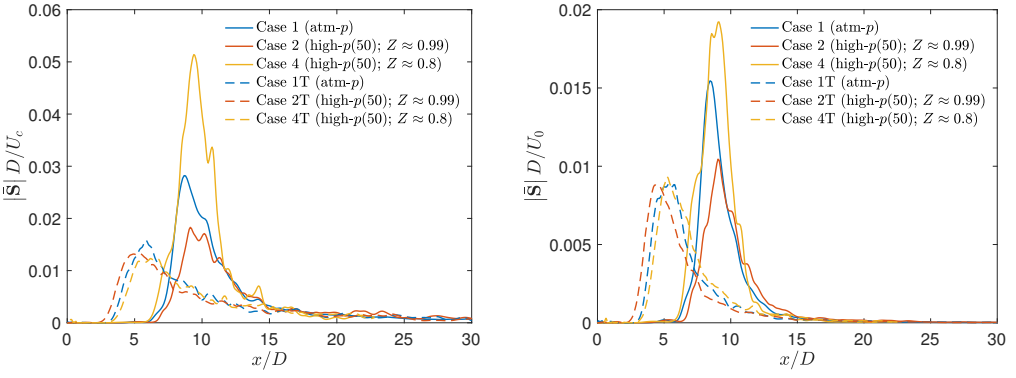

(a) (b)

FIGURE 38. Centerline variation of strain rate magnitude, $|\bar{\mathbf{S}}|$, normalized by (a) U_c/D and (b) U_0/D .

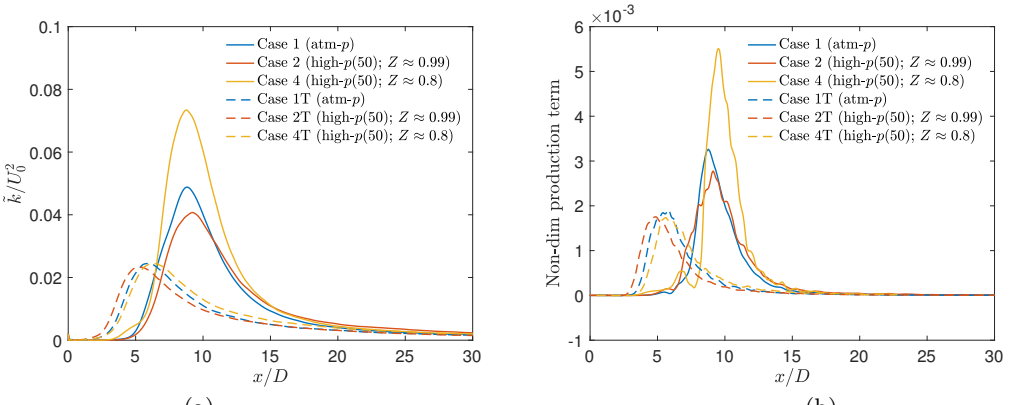

(a) (b)

FIGURE 39. Centerline variation of (a) Favre-averaged t.k.e. normalized by U_0^2 and (b) t.k.e. production term (5.24) normalized by ρ_e (jet-exit density), U_0 and D.

velocity/scalar half-radius spreading rate (figure 13) is larger in the jet from laminar inflow (Case 1) than that from pseudo-turbulent inflow (Case 1T). The normalized self-similar mean axial velocity, $\bar{u}/U_c$, and Reynolds stress components (figure 14) have higher magnitude away from the centerline in the laminar-inflow jet (Case 1) than in that from pseudo-turbulent inflow (Case 1T). The normalized r.m.s. velocity and scalar fluctuations (figures 17 and 30(a)) have a strong hump in the transition region of laminar inflow jet (Case 1), while no such hump occurs in the jet from pseudo-turbulent inflow (Case 1T). Inflow change at high pressure shows similar behavior (§4.5). However, the extent of differences depend on the thermodynamic state that varies with Z. Differences are larger at smaller Z, e.g. between Case 4 and Case 4T.

All considered jet flows, regardless of the thermodynamic and inflow details, exhibit self-similarity of mean axial velocity and Reynolds stress components (figures 20, 31 and 32). This is a new finding for fully-compressible high-p jets. The self-similar profiles are, however, different for individual cases.

Increasing chamber pressure from 1 bar (Case 1/1T) to 50 bar (Case 2/2T), with Z near unity, marginally reduces normalized pressure/density fluctuations. Decreasing Z at a fixed supercritical p_∞ increases the normalized pressure/density fluctuations, independent of the inflow condition (figures 21(a) and 33(a)–(b)). The effect on normalized velocity fluctuations, however, depends on the inflow. Larger mean strain rates in the transition region of the laminar inflow cases enhance turbulent kinetic energy production when Z is decreased from 0.99 (Case 2) to 0.8 (Case 4), while the differences are minimal between Case 2T and Case 4T (figure 30(a)). The dynamics-based compressibility in mixing layers, defined using the convective Mach number, reduces t.k.e. and momentum-thickness growth rate by reducing pressure fluctuations (Vreman *et al.* 1996). In contrast, the influence of Z (at supercritical pressure) on both t.k.e. and the jet spread rate is not exactly correlated with pressure fluctuations, but with the fluctuating pressure-axial-velocity correlation that determines turbulent transport due to pressure fluctuations in the t.k.e. equation. The crucial finding is that p_∞ and Z modify the structure of turbulence through production and transport of t.k.e..

The jet-flow regions and metrics sensitive to p_∞, Z and inflow condition, identified in this study, may guide high-p experimental studies in obtaining measurements that may serve as databases for simulation and model validation. For example, the transition region of laminar-inflow jets exhibits high sensitivity to Z, and thus high-resolution measurements in that region may help evaluate high-p model robustness and accuracy. The results from this study also demonstrate that high-p jet experiments performed at a fixed Z cannot be used to infer results for jets at same Z but larger p_∞.

Acknowledgements

This work was supported at the California Institute of Technology by the Army Research Office under the direction of Dr. Ralph Anthenien. The computational resources were provided by the NASA Advanced Supercomputing at Ames Research Center under the T^3 program directed by Dr. Michael Rogers.

A. Grid convergence

An estimate of the Kolmogorov length scale, η_K, can be made for an incompressible

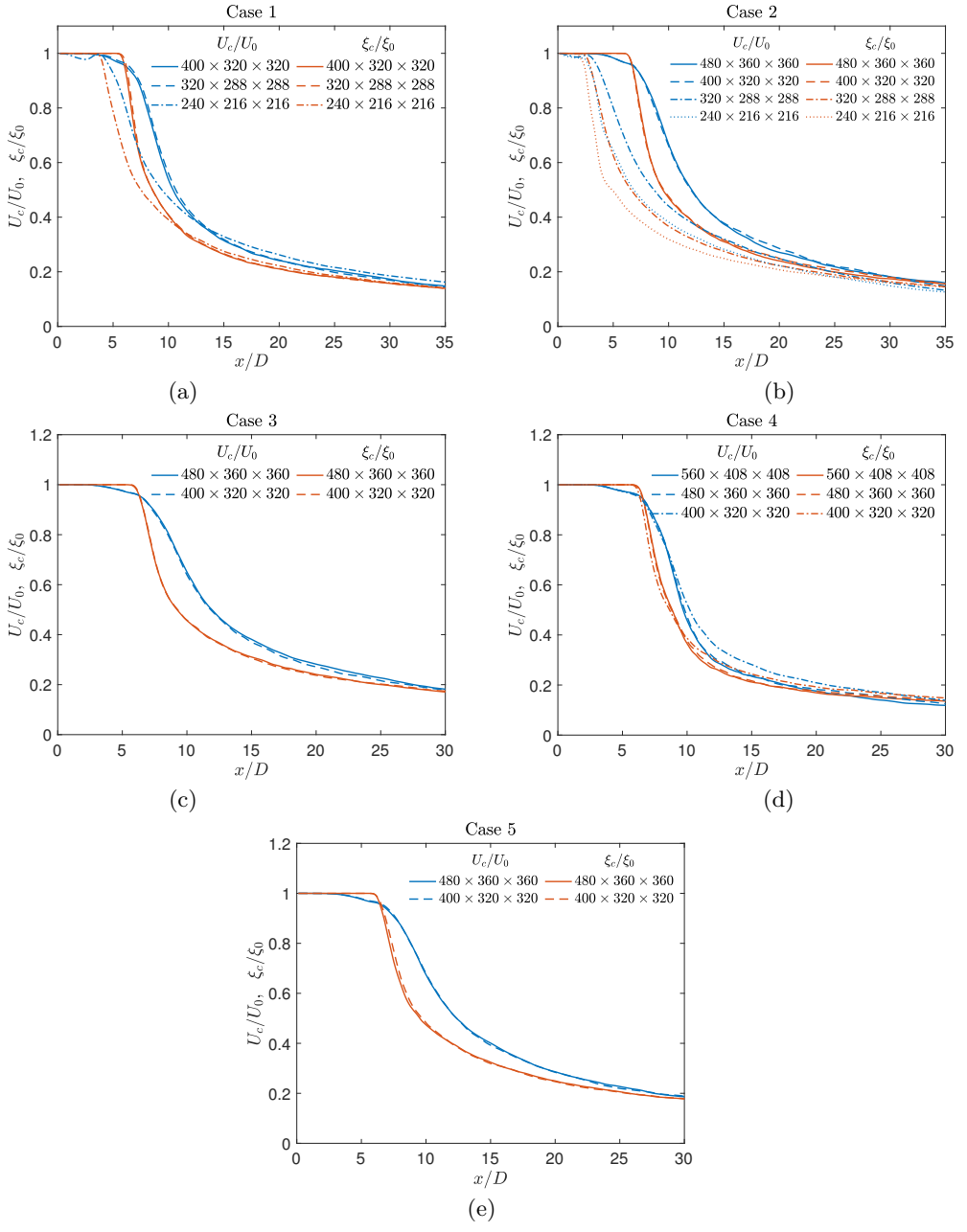

FIGURE 40. Time-averaged centerline velocity (U_c) and scalar (ξ_c) values normalized by the jet exit values U_0 and ξ_0 as a function of axial distance for various grid resolutions. (a) Case 1, (b) Case 2, (c) Case 3, (d) Case 4, and (e) Case 5.

(or weakly compressible) flow by

$$\eta_K = \left(\frac{\nu^3}{\epsilon}\right)^{\frac{1}{4}}, \tag{A 1}$$

where ν is the kinematic viscosity and ϵ denotes the kinetic-energy dissipation. The

dissipation along the centerline in the self-similar region is estimated from (e.g. Panchapakesan & Lumley 1993; Boersma *et al.* 1998)

$$\epsilon = 0.015 \frac{U_c^3(x)}{\delta_{1/2}(x)}, \tag{A 2}$$

where $U_c(x)$ denotes the centerline velocity and $\delta_{1/2}(x)$ is the jet's half-width. For a round jet with top-hat exit velocity profile, the self-similar centerline velocity can be estimated from the empirical relation (4.13) and its half width can be estimated from (e.g. Pope 2001)

$$\delta_{1/2}(x) = S(x - x_{0u}), \tag{A 3}$$

where S is the spreading rate. Substituting (4.13) and (A 3) in (A 2) and in turn substituting (A 2) in (A 1) yields

$$\eta_K = \left(\frac{S}{0.015 B_u^3 Re_D^3} \right)^{\frac{1}{4}} (x - x_{0u}). \tag{A 4}$$

Equation (A 4) shows that the grid should stretch linearly in axial direction in the self-similar regime. While (A 4) provides an estimate of grid spacing, the relations for incompressible flows may not necessarily apply in high-pressure flows of interest here. Therefore, to ensure grid convergence, mean flow statistics are compared in this section by successively refining the grid for Cases 1 to 5 (see table 2), which ensures sufficient grid resolution for DNS.

Figures 40(a) to (e) compare the time-averaged centerline velocity, U_c, and scalar concentration, ξ_c, normalized by the jet exit values U_0 and ξ_0 as a function of axial distance from simulations of Cases 1 to 5 with various grid resolutions. Statistics for Case 1 at atmospheric conditions converges at a resolution of $320 \times 288 \times 288$, whereas, for high-pressure cases, they converge around $400 \times 320 \times 320$, except Case 4 at $Z = 0.8$ having maximum deviation from perfect gas among all cases considered that shows convergence around $480 \times 360 \times 360$. The plots also show that in all cases the scalar concentration begins to decay upstream of the velocity and at a faster rate than the velocity, consistent with the observation of (Lubbers *et al.* 2001, see Figure 6) for a passive scalar diffusing at unity Schmidt number.

B. **Scalar contour plots**

To compare scalar mixing between jets from the laminar and pseudo-turbulent inflow, figure 41 shows the instantaneous mixed fluid contours from Cases 1 and 1T over a slice of the full computational domain. Corresponding near-field images are shown in figure 12.

REFERENCES

Baab, S., Förster, F. J., Lamanna, G. & Weigand, B. 2016 Speed of sound measurements and mixing characterization of underexpanded fuel jets with supercritical reservoir condition using laser-induced thermal acoustics. *Experiments in Fluids* **57** (11), 172.

Baab, S., Steinhausen, C., Lamanna, G., Weigand, B. & Förster, F. J. 2018 A quantitative speed of sound database for multi-component jet mixing at high pressure. *Fuel* **233**, 918–925.

Balaras, E., Piomelli, U. & Wallace, J. M. 2001 Self-similar states in turbulent mixing layers. *Journal of Fluid Mechanics* **446**, 1.

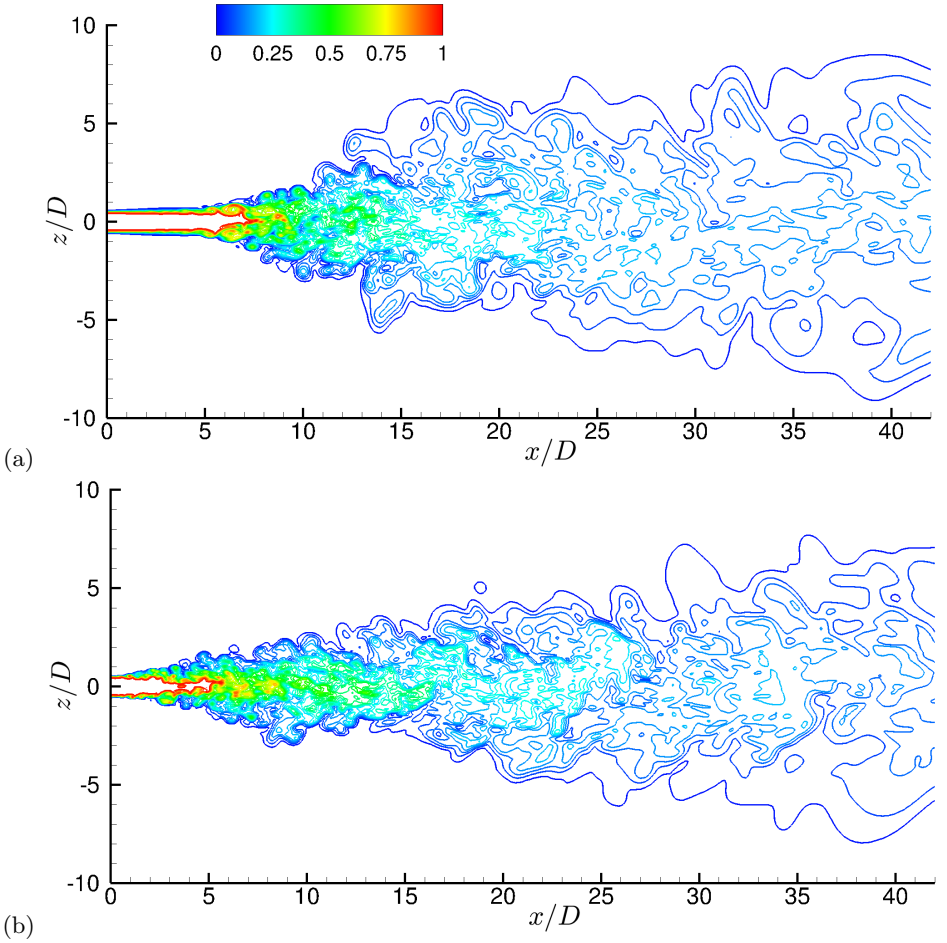

FIGURE 41. Instantaneous scalar contours at $tU_e/D \approx 3500$ from (a) Case 1 and (b) Case 1T showing the mixed fluid concentration. The contour lines show 24 levels in the range $0.02 \leqslant \xi \leqslant 0.98$. The legend is the same for both plots.

BODONY, D. J. 2006 Analysis of sponge zones for computational fluid mechanics. *Journal of Computational Physics* **212** (2), 681–702.

BOERSMA, B. J., BRETHOUWER, G. & NIEUWSTADT, F. 1998 A numerical investigation on the effect of the inflow conditions on the self-similar region of a round jet. *Physics of Fluids* **10** (4), 899–909.

CHEHROUDI, B., TALLEY, D. & COY, E. 2002 Visual characteristics and initial growth rates of round cryogenic jets at subcritical and supercritical pressures. *Physics of Fluids* **14** (2), 850–861.

DOWLING, D. R. & DIMOTAKIS, P. E. 1990 Similarity of the concentration field of gas-phase turbulent jets. *Journal of Fluid Mechanics* **218**, 109–141.

EBRAHIMI, I. & KLEINE, R. 1977 Konzentrationsfelder in isothermen luft-freistrahlen. *Forschung im Ingenieurwesen A* **43** (1), 25–30.

EGGELS, J., UNGER, F., WEISS, M. H., WESTERWEEL, J., ADRIAN, R. J., FRIEDRICH, R. & NIEUWSTADT, F. 1994 Fully developed turbulent pipe flow: a comparison between direct numerical simulation and experiment. *Journal of Fluid Mechanics* **268**, 175–210.

FALGOUT, Z., RAHM, M., WANG, Z. & LINNE, M. 2015 Evidence for supercritical mixing layers in the ECN Spray A. *Proceedings of the Combustion Institute* **35** (2), 1579–1586.

FREUND, J. B., LELE, S. K. & MOIN, P. 2000 Compressibility effects in a turbulent annular

mixing layer. part 1. turbulence and growth rate. *Journal of Fluid Mechanics* **421**, 229–267.

Gao, W., Lin, Y., Hui, X., Zhang, C. & Xu, Q. 2019 Injection characteristics of near critical and supercritical kerosene into quiescent atmospheric environment. *Fuel* **235**, 775–781.

George, W. K. 1989 The self-preservation of turbulent flows and its relation to initial conditions and coherent structures. *Advances in Turbulence* **3973**.

George, W. K. & Davidson, L. 2004 Role of initial conditions in establishing asymptotic flow behavior. *AIAA Journal* **42** (3), 438–446.

Ghosal, S. & Rogers, M. M. 1997 A numerical study of self-similarity in a turbulent plane wake using large-eddy simulation. *Physics of Fluids* **9** (6), 1729–1739.

Grinstein, F. F. 2001 Vortex dynamics and entrainment in rectangular free jets. *Journal of Fluid Mechanics* **437**, 69–101.

Harstad, K. G., Miller, R. S. & Bellan, J. 1997 Efficient high-pressure state equations. *AIChE Journal* **43** (6), 1605–1610.

Ho, C. M. & Nosseir, N. S. 1981 Dynamics of an impinging jet. part 1. the feedback phenomenon. *Journal of Fluid Mechanics* **105**, 119–142.

Huang, P. C., Coleman, G. N. & Bradshaw, P. 1995 Compressible turbulent channel flows: Dns results and modelling. *Journal of Fluid Mechanics* **305**, 185–218.

Husain, Z. D. & Hussain, A. K. M. F. 1979 Axisymmetric mixing layer: influence of the initial and boundary conditions. *AIAA Journal* **17** (1), 48–55.

Hussein, H. J., Capp, S. P. & George, W. K. 1994 Velocity measurements in a high-reynolds-number, momentum-conserving, axisymmetric, turbulent jet. *Journal of Fluid Mechanics* **258**, 31–75.

Kennedy, C. A. & Carpenter, M. H. 1994 Several new numerical methods for compressible shear-layer simulations. *Applied Numerical Mathematics* **14** (4), 397–433.

Klein, M., Sadiki, A. & Janicka, J. 2003 A digital filter based generation of inflow data for spatially developing direct numerical or large eddy simulations. *Journal of Computational Physics* **186** (2), 652–665.

Lele, S. K. 1994 Compressibility effects on turbulence. *Annual Review of Fluid Mechanics* **26** (1), 211–254.

Lemmon, E. W., Huber, M. L., McLinden, M. O. & others 2010 NIST standard reference database 23. *NIST Reference Fluid Thermodynamic and Transport PropertiesREFPROP, Version* **9**, 55.

Lodato, G., Domingo, P. & Vervisch, L. 2008 Three-dimensional boundary conditions for direct and large-eddy simulation of compressible viscous flows. *Journal of Computational Physics* **227** (10), 5105–5143.

Lubbers, C. L., Brethouwer, G. & Boersma, B. J. 2001 Simulation of the mixing of a passive scalar in a round turbulent jet. *Fluid Dynamics Research* **28** (3), 189.

Lund, T. S., Wu, X. & Squires, K. D. 1998 Generation of turbulent inflow data for spatially-developing boundary layer simulations. *Journal of Computational Physics* **140** (2), 233–258.

Masi, E., Bellan, J., Harstad, K. G. & Okong'o, N. A 2013 Multi-species turbulent mixing under supercritical-pressure conditions: modelling, direct numerical simulation and analysis revealing species spinodal decomposition. *Journal of Fluid Mechanics* **721**, 578–626.

Mattner, T. W. 2011 Large-eddy simulations of turbulent mixing layers using the stretched-vortex model. *Journal of Fluid Mechanics* **671**, 507–534.

Mayer, W., Schik, A., Axel H., Vielle, B., Chauveau, C., G-ograve, I., kalp, Talley, D. G. & Woodward, R. D 1998 Atomization and breakup of cryogenic propellants under high-pressure subcritical and supercritical conditions. *Journal of Propulsion and Power* **14** (5), 835–842.

Mayer, W., Telaar, J., Branam, R., Schneider, G. & Hussong, J. 2003 Raman measurements of cryogenic injection at supercritical pressure. *Heat and Mass Transfer* **39** (8-9), 709–719.

Mi, J., Nobes, D. S. & Nathan, G. J. 2001 Influence of jet exit conditions on the passive scalar field of an axisymmetric free jet. *Journal of Fluid Mechanics* **432**, 91–125.

Michalke, A. 1984 Survey on jet instability theory. *Progress in Aerospace Sciences* **21**, 159–199.

Morris, Philip J 1983 Viscous stability of compressible axisymmetric jets. *AIAA Journal* **21** (4), 481–482.

Muthukumaran, C. K. & Vaidyanathan, A. 2016*a* Initial instability of round liquid jet at subcritical and supercritical environments. *Physics of Fluids* **28** (7), 074104.

Muthukumaran, C. K. & Vaidyanathan, A. 2016*b* Mixing nature of supercritical jet in subcritical and supercritical conditions. *Journal of Propulsion and Power* **33** (4), 842–857.

Newman, J. A. & Brzustowski, T. A. 1971 Behavior of a liquid jet near the thermodynamic critical region. *AIAA Journal* **9** (8), 1595–1602.

Okong'o, N. & Bellan, J. 2002*a* Consistent boundary conditions for multicomponent real gas mixtures based on characteristic waves. *Journal of Computational Physics* **176** (2), 330–344.

Okong'o, N. A. & Bellan, J. 2002*b* Direct numerical simulation of a transitional supercritical binary mixing layer: heptane and nitrogen. *Journal of Fluid Mechanics* **464**, 1–34.

Okong'o, N. A., Harstad, K. & Bellan, J. 2002 Direct numerical simulations of o2/h2 temporal mixing layers under supercritical conditions. *AIAA Journal* **40** (5), 914–926.

Oschwald, M. & Schik, A. 1999 Supercritical nitrogen free jet investigated by spontaneous raman scattering. *Experiments in Fluids* **27** (6), 497–506.

Panchapakesan, N. R. & Lumley, J. L. 1993 Turbulence measurements in axisymmetric jets of air and helium. part 1. air jet. *Journal of Fluid Mechanics* **246**, 197–223.

Pantano, C. & Sarkar, S. 2002 A study of compressibility effects in the high-speed turbulent shear layer using direct simulation. *Journal of Fluid Mechanics* **451**, 329–371.

Papamoschou, D. & Roshko, A. 1988 The compressible turbulent shear layer: an experimental study. *Journal of Fluid Mechanics* **197**, 453–477.

Poinsot, T. J. & Lele, S. K. 1992 Boundary conditions for direct simulations of compressible viscous flows. *Journal of Computational Physics* **101** (1), 104–129.

Poling, B. E., Prausnitz, J. M., O'connell, J. P. & others 2001 *The properties of gases and liquids*, , vol. 5. Mcgraw-Hill New York.

Pope, S. B. 2001 *Turbulent flows*. IOP Publishing.

Poursadegh, F., Lacey, J. S., Brear, M. J. & Gordon, R. L. 2017 On the fuel spray transition to dense fluid mixing at reciprocating engine conditions. *Energy & Fuels* **31** (6), 6445–6454.

Richards, C. D. & Pitts, W. M. 1993 Global density effects on the self-preservation behaviour of turbulent free jets. *Journal of Fluid Mechanics* **254**, 417–435.

Ries, F., Obando, P., Shevchuck, I., Janicka, J. & Sadiki, A. 2017 Numerical analysis of turbulent flow dynamics and heat transport in a round jet at supercritical conditions. *International Journal of Heat and Fluid Flow* **66**, 172–184.

Roy, A., Joly, C. & Segal, C. 2013 Disintegrating supercritical jets in a subcritical environment. *Journal of Fluid Mechanics* **717**, 193–202.

Schmitt, T., Selle, L., Ruiz, A. & Cuenot, B. 2010 Large-eddy simulation of supercritical-pressure round jets. *AIAA Journal* **48** (9), 2133–2144.

Sciacovelli, L. & Bellan, J. 2019 The influence of the chemical composition representation according to the number of species during mixing in high-pressure turbulent flows. *Journal of Fluid Mechanics* **863**, 293–340.

Segal, C. & Polikhov, S. A. 2008 Subcritical to supercritical mixing. *Physics of Fluids* **20** (5), 052101.

Selle, L. & Schmitt, T. 2010 Large-eddy simulation of single-species flows under supercritical thermodynamic conditions. *Combustion Science and Technology* **182** (4-6), 392–404.

Sharan, N. 2016 Time-stable high-order finite difference methods for overset grids. PhD thesis, University of Illinois at Urbana-Champaign.

Sharan, N., Matheou, G. & Dimotakis, P. E. 2018*a* Mixing, scalar boundedness, and numerical dissipation in large-eddy simulations. *Journal of Computational Physics* **369**, 148–172.

Sharan, N., Matheou, G. & Dimotakis, P. E. 2019 Turbulent shear-layer mixing: initial conditions, and direct-numerical and large-eddy simulations. *Journal of Fluid Mechanics* **877**, 35–81.

Sharan, N., Pantano, C. & Bodony, D. J. 2018*b* Time-stable overset grid method for

hyperbolic problems using summation-by-parts operators. *Journal of Computational Physics* **361**, 199–230.

Simone, A., Coleman, G. N. & Cambon, C. 1997 The effect of compressibility on turbulent shear flow: a rapid-distortion-theory and direct-numerical-simulation study. *Journal of Fluid Mechanics* **330**, 307–338.

Slessor, M. D., Bond, C. L. & Dimotakis, P. E. 1998 Turbulent shear-layer mixing at high reynolds numbers: effects of inflow conditions. *Journal of Fluid Mechanics* **376**, 115–138.

Taşkinoğlu, E. S. & Bellan, J. 2010 A posteriori study using a dns database describing fluid disintegration and binary-species mixing under supercritical pressure: heptane and nitrogen. *Journal of Fluid Mechanics* **645**, 211–254.

Taşkinoğlu, E. S. & Bellan, J. 2011 Subgrid-scale models and large-eddy simulation of oxygen stream disintegration and mixing with a hydrogen or helium stream at supercritical pressure. *Journal of Fluid Mechanics* **679**, 156–193.

Townsend, A. 1980 *The structure of turbulent shear flow*. Cambridge University Press.

Vreman, A. W., Sandham, N. D. & Luo, K. H. 1996 Compressible mixing layer growth rate and turbulence characteristics. *Journal of Fluid Mechanics* **320**, 235–258.

Woodward, R. & Talley, D. 1996 Raman imaging of transcritical cryogenic propellants. In *34th Aerospace Sciences Meeting and Exhibit*, p. 468.

Wygnanski, I., Champagne, F. & Marasli, B. 1986 On the large-scale structures in two-dimensional, small-deficit, turbulent wakes. *Journal of Fluid Mechanics* **168**, 31–71.

Wygnanski, I. & Fiedler, H. O. 1969 Some measurements in the self-preserving jet. *Journal of Fluid Mechanics* **38** (3), 577–612.

Xu, G. & Antonia, R. 2002 Effect of different initial conditions on a turbulent round free jet. *Experiments in Fluids* **33** (5), 677–683.